



X-BASE: the first terrestrial carbon and water flux products from an extended data-driven scaling framework, FLUXCOM-X

Jacob A Nelson^{1,*}, Sophia Walther^{1,*}, Fabian Gans¹, Basil Kraft¹, Ulrich Weber¹, Kimberly Novick², Nina Buchmann³, Mirco Migliavacca⁴, Georg Wohlfahrt⁵, Ladislav Šigut⁶, Andreas Ibrom⁷, Dario Papale^{8,9}, Mathias Göckede¹, Gregory Duveiller¹, Alexander Knöhl^{10,11}, Lukas Hörtnagl³, Russell L. Scott¹², Weijie Zhang¹, Zayd Mahmoud Hamdi¹, Markus Reichstein^{1,13}, Sergio Aranda-Barranco^{14,15}, Jonas Ardö¹⁶, Maarten Op de Beeck^{17,18}, Dave Billesbach¹⁹, David Bowling²⁰, Rosvel Bracho²¹, Christian Brümmer²², Gustau Camps-Valls²³, Shiping Chen²⁴, Jamie Rose Cleverly²⁵, Ankur Desai²⁶, Gang Dong²⁷, Tarek S. El-Madany¹, Eugenie Susanne Euskirchen²⁸, Iris Feigenwinter³, Marta Galvagno²⁹, Giacomo Al. Gerosa³⁰, Bert Gielen³¹, Ignacio Goded⁴, Sarah Goslee³², Christopher Michael Gough³³, Bernard Heinesch³⁴, Kazuhito Ichii³⁵, Marcin Antoni Jackowicz-Korczynski^{36,37}, Anne Klosterhalfen³⁸, Sara Knox^{39,40}, Hideki Kobayashi⁴¹, Kukka-Maaria Kohonen³, Mika Korkiakoski⁴², Ivan Mammarella⁴³, Gharun Mana⁴⁴, Riccardo Marzuoli⁴⁵, Roser Matamala^{46,47,48}, Stefan Metzger^{49,50}, Leonardo Montagnani⁵¹, Giacomo Nicolini⁹, Thomas O'Halloran^{52,53}, Jean-Marc Ourcival⁵⁴, Matthias Peichl⁵⁵, Elise Pendall⁵⁶, Borja Ruiz Reverte⁵⁷, Marilyn Roland⁵⁸, Simone Sabbatini^{9,59}, Torsten Sachs⁶⁰, Marius Schmidt⁶¹, Christopher R Schwalm⁶², Ankit Shekhar³, Richard Silberstein⁶³, Maria Lucia Silveira⁶⁴, Donatella Spano^{65,9}, Torben Tagesson^{66,67}, Gianluca Tramontana⁶⁸, Carlo Trotta⁹, Fabio Turco³, Timo Vesala^{69,70}, Caroline Vincke⁷¹, Domenico Vitale⁷², Enrique R. Vivoni^{73,74}, Yi Wang³, William Woodgate^{75,76}, Enrico A. Yepez⁷⁷, Junhui Zhang^{78,79}, Donatella Zona⁸⁰, and Martin Jung¹

*These authors contributed equally to this work.

¹Max-Planck-Institute for Biogeochemistry, Germany

²O'Neill School of Public and Environmental Affairs, Indiana University - Bloomington (USA)

³Department of Environmental Systems Science, ETH Zurich, 8092 Zurich, Switzerland

⁴European Commission, Joint Research Centre, Ispra (Varese), Italy

⁵Universität Innsbruck, Institut für Ökologie, Sternwartestrasse 15, 6020 Innsbruck, AUSTRIA

⁶Global Change Research Institute CAS, Bělidla 986/4a, CZ-60300 Brno, Czech Republic

⁷Department of Environment and Resource Engineering, Technical University of Denmark (DTU), Bygningstorvet 115, 2800 Kgs. Lyngby, Denmark

⁸Research Institute on Terrestrial Ecosystems (IRET), National Research Council (CNR), 00010 Montelibretti (Roma), Italy

⁹CMCC Foundation - Euro-Mediterranean Center on Climate Change, Italy

¹⁰University of Goettingen, Bioclimatology, Faculty of Forest Sciences, 37077 Göttingen, Germany.

¹¹University of Goettingen, Centre of Biodiversity and Sustainable Land Use (CBL), 37077 Göttingen, Germany

¹²Southwest Watershed Research Center, USDA-ARS, Tucson, AZ

¹³German Centre for Integrative Biodiversity Research (iDiv) Halle-Jena-Leipzig, Leipzig, Germany

¹⁴Department of Ecology, University of Granada, Granada, Spain

¹⁵Andalusian Institute for Earth System Research (CEAMA-IISTA), University of Granada, Granada, Spain

¹⁶Department of Physical Geography and Ecosystem Science Sölvegatan 12 223 62 Lund, Sweden

¹⁷Research Group Plants and Ecosystems, Department of Biology, University of Antwerp

¹⁸ICOS / Ecosystem Thematic Centre

¹⁹University of Nebraska-Lincoln, School of Natural Resources (Retired)



²⁰School of Biological Sciences, University of Utah
²¹School of Forest, Fisheries, and Geomatics Sciences University of Florida, Gainesville, FL, 32611, USA
²²Thünen Institute of Climate-Smart Agriculture, Braunschweig, Germany
²³Image Processing Laboratory (IPL), Universitat de València, Spain
²⁴State Key Laboratory of Vegetation and Environmental Change, Institute of Botany, Chinese Academy of Sciences, Beijing 100093, P. R. China
²⁵College of Science and Engineering, James Cook University, Cairns, Queensland, Australia
²⁶Dept of Atmospheric and Oceanic Sciences, University of Wisconsin-Madison, Madison, WI 53706 USA
²⁷Shanxi University, China
²⁸University of Alaska Fairbanks, Institute of Arctic Biology, Fairbanks, AK 99775, USA
²⁹Environmental Protection Agency of Aosta Valley, Climate Change Unit, (ARPA Valle d'Aosta), Italy
³⁰Dept. of Mathematics and Physics, Catholic University of the Sacred Heart, Brescia (Italy)
³¹Plants and Ecosystems (PLECO), Department of Biology, University of Antwerp, B-2610 Wilrijk, Belgium
³²USDA-ARS
³³Virginia Commonwealth University, Department of Biology
³⁴Terra Teaching and Research Center, University of Liège – Gembloux Agro-Bio Tech, 5030 Gembloux, Belgium.
³⁵Center for Environmental Remote Sensing, Chiba University, Japan
³⁶Department of Ecosystems, Aarhus University, Frederiksbergvej 399, Roskilde 4000, Denmark
³⁷Department of Physical Geography and Ecosystem Science, Lund University, Sölvegatan 12, 223 62 Lund, Sweden
³⁸Bioclimatology, University of Goettingen, 37077 Goettingen, Germany
³⁹Department of Geography, McGill University, Montreal, Canada
⁴⁰Department of Geography, The University of British Columbia, Vancouver, Canada
⁴¹Research Institute for Global Change, Japan Agency for Marine-Earth Science and Technology
⁴²Finnish Meteorological Institute, Climate System Research Unit, P.O. Box 503, 00101 Helsinki, Finland
⁴³Institute of Atmospheric and Earth System Research / Physics, University of Helsinki, Helsinki, Finland
⁴⁴Institute of Landscape Ecology, University of Münster, Münster, Germany
⁴⁵Catholic University of the Sacred Heart, Dep. of Mathematics and Physics, via Garzetta 48 Brescia, Italy
⁴⁶Environmental Science Division, Argonne National Laboratory, Lemont, IL, USA
⁴⁷University of Chicago Consortium for Advanced Science & Engineering (CASE), Chicago, IL, USA
⁴⁸Northwestern Argonne Institute of Science and Engineering, Evanston, IL, USA
⁴⁹National Ecological Observatory Network, Battelle, 1685 38th Street, 80301 Boulder, CO, USA
⁵⁰Department of Atmospheric and Oceanic Sciences, University of Wisconsin-Madison, 1225 W Dayton St, 53711 Madison, WI, USA
⁵¹Free University of Bolzano, Faculty of Agricultural, Environmental and Food Sciences - Universitätsplatz 1 - Piazza Università, 1 39100 Bozen-Bolzano
⁵²Belle W. Baruch Institute of Coastal Ecology and Forest Science, Clemson University, Georgetown, SC, United States
⁵³Forestry and Environmental Conservation Department, Clemson University, Clemson, SC, United States
⁵⁴CEFE, Univ Montpellier, CNRS, EPHE, IRD, Montpellier, France
⁵⁵Department of Forest Ecology and Management, Swedish University of Agricultural Sciences, Skogsmarksgränd 17, SE-901 83, Umeå, Sweden
⁵⁶Hawkesbury Institute for the Environment, Western Sydney University, Penrith Australia 2751
⁵⁷Departamento de Química e Física, Universidade Federal da Paraíba - Campus II, 58397-000 Areia, Paraíba, Brazil
⁵⁸Plants and Ecosystems, Department of Biology, University of Antwerp, 2610 Wilrijk, Belgium
⁵⁹University of Tuscia, Department for Innovation in Biological, Agro-food and Forest Systems (DIBAF)
⁶⁰GFZ German Research Centre for Geosciences, Potsdam, Germany
⁶¹Forschungszentrum Jülich, Institute of Bio-and Geosciences: Agrosphere (IBG-3), 52428 Jülich, Germany
⁶²Woodwell Climate Research Center: FALMOUTH, MA, US
⁶³School of Science, Edith Cowan University, Australia
⁶⁴University of Florida, Range Cattle Research and Education Center. 3401 Experiment Station, Ona, FL, USA 33865.



⁶⁵Department of Agriculture Sciences, University of Sassari, Italy

⁶⁶Department of Physical Geography and Ecosystem Science, Lund University, Sölvegatan 12, SE-223 62 Lund, Sweden

⁶⁷Department of Geosciences and Natural Resource Management, University of Copenhagen, Øster Voldgade 10, DK-1350 Copenhagen, Denmark

⁶⁸Terrasystem srl

⁶⁹Institute for Atmospheric and Earth System Research/Physics, Faculty of Science, University of Helsinki, Helsinki, 00014, Finland

⁷⁰Institute for Atmospheric and Earth System Research/Forest Sciences, Faculty of Agriculture and Forestry, University of Helsinki, Helsinki, 00014, Finland

⁷¹UCLouvain - Erath and Life Institute (ELI) Croix du Sud, 2 bte L7.05.24 (de Serres B249) 2013 1348 Louvain-la-Neuve

⁷²Department of Methods and Models for Economics, Territory and Finance (MEMOTEF), Sapienza University of Rome, Via del Castro Laurenziano, 9, 00161, Rome, Italy

⁷³School of Sustainable Engineering and the Built Environment, Arizona State University, Tempe, AZ, USA 85287-8704

⁷⁴Center for Hydrologic Innovations, Arizona State University, Tempe, AZ, USA 85287-8704

⁷⁵School of the Environment, The University of Queensland, 4072, Australia

⁷⁶CSIRO, Space and Astronomy, Kensington, 6151, WA, Australia

⁷⁷Instituto Tecnológico de Sonora, 5 de Febrero 818 Sur, Col. Centro, Cd. Obregon, Sonora, México, 85000

⁷⁸School of life sciences, University of Qufu normal university, Qufu 273165, Shandong, China

⁷⁹Institute of Applied Ecology, Chinese Academy of Sciences, Shenyang 110016, China

⁸⁰Department Biology, San Diego State University, San Diego, CA 92182, USA

Correspondence: Jacob A Nelson (jnelson@bgc-jena.mpg.de) and Sophia Walther (sophia.walther@bgc-jena.mpg.de)

Abstract. Mapping in-situ eddy covariance measurements of terrestrial land-atmosphere fluxes to the globe is a key method for diagnosing the Earth system from a data-driven perspective. We describe the first global products (called X-BASE) from a newly implemented up-scaling framework, FLUXCOM-X. The X-BASE products comprise of estimates of CO_2 net ecosystem exchange (NEE), gross primary productivity (GPP) as well as evapotranspiration (ET) and, for the first time, a novel

5 fully data-driven global transpiration product (ET_T), at high spatial (0.05°) and temporal (hourly) resolution. X-BASE estimates the global NEE at $-5.75 \pm 0.33 \text{ PgC yr}^{-1}$ for the period 2001-2020, showing a much higher consistency with independent atmospheric carbon cycle constraints compared to the previous versions of FLUXCOM. The improvement of global NEE was likely only possible thanks to the international effort to increase the precision and consistency of eddy covariance collection and processing pipelines, as well as to the extension of the measurements to more site-years resulting in a 10 wider coverage of bio-climatic conditions. However, X-BASE global net ecosystem exchange shows a very low inter-annual variability, which is common to state-of-the-art data-driven flux products and remains a scientific challenge. With $125 \pm 2.1 \text{ PgC yr}^{-1}$ for the same period, X-BASE GPP is slightly higher than previous FLUXCOM estimates, mostly in temperate and boreal areas. X-BASE evapotranspiration amounts to $74.7 \times 10^3 \pm 0.9 \times 10^3 \text{ km}^3$ globally for the years 2001-2020, but exceeds precipitation in many dry areas likely indicating overestimation in these regions. On average 57% of evapotranspiration 15 are estimated to be transpiration, in good agreement with isotope-based approaches, but higher than estimates from many land surface models. Despite considerable improvements to the previous up-scaling products, many further opportunities for development exist. Pathways of exploration include methodological choices in the selection and processing of eddy-covariance and satellite observations, their ingestion into the framework, and the configuration of machine learning methods. For this, the new



FLUXCOM-X framework was specifically designed to have the necessary flexibility to experiment, diagnose, and converge to
20 more accurate global flux estimates.

1 Introduction

Energy, water, and carbon exchange between terrestrial surfaces and the atmosphere are key components of the Earth system and impact ecosystems, ecosystem services, weather, climate, and water availability. The exchange (or flux) can be directly observed using eddy covariance (EC) measurement systems (Baldocchi, 2019) which are installed on towers overlooking the
25 ecosystem of interest. The EC stations typically represent an area of a few hundred square meters to a square kilometer. One key advantage of the EC methodology is the ability to provide near continuous measurements with some records now exceeding 20 years (Pastorello et al., 2020), allowing for examination of flux variations from the order of thirty minutes to decades. EC systems also provide a unique perspective on the magnitude, temporal variability, and environmental sensitivity of ecosystem CO_2 uptake, water use, and local climate regulation (Baldocchi, 2019; Musavi et al., 2017; Bao et al., 2022).
30 However, while many of the most pressing scientific knowledge gaps surrounding the delicate land carbon balance and the water cycle require spatially and temporally resolved flux patterns at continental to global scales, EC observations are confined to individual locations in space and limited periods in time (Kumar et al., 2016; Papale et al., 2015). Methodologies to transcend the gap between local and global scales are needed to ultimately support societal relevant activities of building greenhouse gas monitoring systems, taking informed climate and land management actions, and verifying the effectiveness of mitigation
35 strategies (Baldocchi and Penuelas, 2019; Bonan et al., 2011; Novick et al., 2022).

Coordinated and consolidated data collections from EC networks are invaluable for the mapping of in-situ fluxes to regional and global scales. For example, EC measurements aid both the parameterization (Huang et al., 2021) and the validation (Turner et al., 2006; Heinsch et al., 2006) of mechanistic models of ecosystem productivity and land surface processes. The latter generate widely used reference data sets for terrestrial carbon cycle applications (Zhao and Running, 2010; Ukkola et al.,
40 2022). A complementary approach to modeling terrestrial fluxes at continental and global scales is of empirical nature and links observations of explanatory variables at the EC stations, particularly meteorological and remote sensing data, to the EC fluxes via machine learning models. This up-scaling concept does not prescribe any mechanistic formulations and assumes that the EC observations cover all complexities of ecosystem functioning. Based on a trained machine learning model and globally gridded input data of the explanatory variables, EC fluxes can be mapped to the global scale.

45 First implementations of this flux up-scaling concept emerged in the early 2000s. They focused on net ecosystem exchange of CO_2 (NEE) and utilized the growing EC networks in Europe (Papale and Valentini, 2003) and North America (Xiao et al., 2008). The release of the La Thuile Synthesis Dataset of harmonized EC data in 2007, as well as methodological improvements in the training of the machine learning models (Jung et al., 2009), led to the first global products of terrestrial CO_2 and water fluxes at a monthly time step and in 0.5° grids in 2011 (Jung et al., 2011). While good agreement of flux estimates derived from complementary process-based models with the up-scaled global gross photosynthetic CO_2 uptake (gross primary productivity, GPP) and energy fluxes demonstrated the potential of the approach, important inconsistencies
50



remained, in particular regarding the globally integrated *NEE* and its year-to-year variability. (Jung et al., 2020, 2019, 2011; Zscheischler et al., 2017).

In an effort to better understand the uncertainties associated with mapping of EC fluxes to larger scales, the FLUXCOM inter-comparison initiative built an ensemble of flux estimates as a type of factorial experiment (Tramontana et al., 2016; Jung et al., 2019, 2020). The ensemble consisted of multiple machine learning algorithms, meteorological forcing data, and combinations of predictor variables resulting in 120 individual up-scaled estimates per flux. These were summarized in two overall ensemble configurations, which differed in the set of predictors and spatial-temporal resolution. Apart from creating a large ensemble, the FLUXCOM evaluation included a consistent site-level cross-validation analysis as well as cross-consistency checks with terrestrial flux estimates from independent approaches, such as complementary modeling concepts or observational surrogates. From a methodological point of view, the key lessons learned from FLUXCOM were that: (1) the overall approach seems to be primarily limited by the input information given to the machine learning algorithms rather than to the ability of the algorithm to extract the information; (2) the largest qualitative differences among flux products were related to the set of the predictor variables rather than to the choice of the machine learning method or meteorological forcing; (3) the cross-consistency checks with global independent data are essential for supplementing site-level cross-validation; and (4) the largest qualitative discrepancy with independent data was a very high (strongly negative) tropical *NEE* that was shared among all ensemble members.

By today, the empirical up-scaling concept has been implemented for a series of regional and global scale applications, each of them adopting disparate and individual methodological choices (e.g. Ichii et al., 2017; Yao et al., 2018; Joiner and Yoshida, 2020; Virkkala et al., 2021; Dannenberg et al., 2023; Burton et al., 2023). These potentially important choices relate to data treatment (quality control, gap-filling, processing pathways), ingestion (sampling, as well as matching EC and space-born observations), and methodological configurations (machine learning methods and their training configuration, choice of predictor variables, resolution). Hence, flexibility to explore the large methodological space, as well as the ability to diagnose and evaluate global products in parallel to site-level cross-validation, are required to make progress in empirical up-scaling of EC fluxes. Learning from key insights in FLUXCOM and other up-scaling exercises further implies striving for enhancing the information content of the training data with aspects related to coverage and quality of EC measurements as well as quality, complementarity, and completeness of predictor variables.

We are developing a modeling framework that allows experimenting with and systematically exploring many of these methodological choices. We coin this extended and flexibly adjustable up-scaling framework FLUXCOM-X. Based on FLUXCOM-X, the latency with which innovations in the related fields of machine learning and spacebased Earth observations as well as novel EC data can find their way to empirical flux up-scaling will be considerably reduced. This in turn allows faster progress towards more accurate and fit-for-the-purpose global biogenic flux estimates. Here, we introduce and evaluate the initial “basic” set of products from this framework, which we refer to as FLUXCOM-X-BASE products (or X-BASE for short).

X-BASE products were generated based on the same principle as in the original FLUXCOM ensemble using qualitatively similar predictor variables, i.e. remotely sensed vegetation indices and land surface temperatures from the Moderate Resolution Imaging Spectroradiometer (MODIS) along with meteorological variables. We made efforts to provide more and improved



information to the machine learning models by enhancing coverage and quality of the training data in X-BASE, and by further developing the processing of satellite predictor variables (Walther and Besnard et al., 2022). In this manuscript, we show results for X-BASE *NEE*, *GPP*, evapotranspiration (*ET*), and for the first time transpiration (*ET_T*), for the period 2001-90 2020 at 0.05° spatial and hourly temporal resolution. X-BASE products are freely available and serve as a baseline for future FLUXCOM-X developments. We are focusing here on the evaluation and cross-consistency checks of X-BASE with previous FLUXCOM products and independent data streams. Our specific objectives are:

1. to describe the production of X-BASE products;
2. to evaluate the X-BASE setup using site-level cross-validation;
- 95 3. to assess qualitative differences of global patterns compared to previous FLUXCOM products with reference to independent flux estimates where possible; and
4. to synthesize lessons learned from this exercise to guide future FLUXCOM-X developments.

2 Data and Methods

The following section gives an overview on the essential methodological implementations and data choices adopted in the 100 generation of X-BASE products.

2.1 Eddy Covariance Data

Eddy covariance data consisted of 294 sites from around the world though skewed towards higher representation from temperate forests from North America and Europe. All EC data were collected, processed, analyzed for quality by the station teams, before being processed using state-of-the-art approaches in the ONEFLUX data processing pipeline (Pastorello et al., 2020). 105 The data included was collected between 2001-2020 and available with a CC BY 4.0 license. Based on this criterion, data for each site came from one of five different sources based on most recent availability: FLUXNET 2015 (Pastorello et al., 2020), ICOS Drought 2018 (Team and Centre, 2020), ICOS Warm Winter 2020 (Team and Centre, 2022), or the most recent Ameriflux or ICOS release as of December 2022. Table 1 lists all sites included as well as the associated digital object identifier specific to the associated release.

Table 1: Citation data for the 294 sites used in the X-BASE products.

AR-SLu(Garcia et al., 2016)	AR-TF1(Kutzbach, 2021)	AR-Vir(Posse et al., 2016)	AT-Neu(Wohlfahrt et al., 2016)	AU-ASM(Cleverly et al., 2016)	AU-Ade(Beringer and Hutley, 2016c)
					2016b)



Table 1: **Citation data for the 294 sites used in the X-BASE products.**

AU-Cpr(Meyer et al., 2016)	AU-Cum(Pendall and Griebel, 2016)	AU-DaP(Beringer and Hutley, 2016b)	AU-DaS(Beringer and Hutley, 2016f)	AU-Dry(Beringer and Hutley, 2016e)	AU-Emr(Schroder et al., 2016)
AU-Fog(Beringer and Hutley, 2016a)	AU-Gin(Macfarlane et al., 2016)	AU-RDF(Beringer and Hutley, 2016d)	AU-Rob(Liddell, 2016)	AU-TTE(Cleverly and Eamus, 2016a)	AU-Tum(Woodgate et al., 2016)
AU-Wac(Beringer et al., 2016b)	AU-Whr(Beringer et al., 2016a)	AU-Wom(Arndt et al., 2016)	AU-Ync(Beringer and Walker, 2016)	BE-Bra(Team and Centre, 2022)	BE-Dor(Team and Centre, 2022)
BE-Lcr(RI, 2021)	BE-Lon(Team and Centre, 2022)	BE-Maa(Team and Centre, 2022)	BE-Vie(Team and Centre, 2022)	BR-Npw(Vourlitis et al., 2022)	BR-Sa1(Saleska, 2016)
BR-Sa3(Goulden, 2016d)	CA-Cbo(Staebler, 2022)	CA-DB2(Knox, 2022)	CA-DBB(Christen and Knox, 2022)	CA-ER1(Wagner-Riddle, 2021)	CA-Gro(McCaughey, 2016)
CA-LP1(Black, 2021)	CA-Man(Amilo, 2016b)	CA-NS2(Goulden, 2016a)	CA-NS3(Goulden, 2016b)	CA-NS4(Goulden, 2016c)	CA-NS5(Goulden, 2016g)
CA-NS6(Goulden, 2016e)	CA-NS7(Goulden, 2016f)	CA-Oas(Black, 2016b)	CA-Obs(Black, 2016a)	CA-Qfo(Margolis, 2016)	CA-SF1(Amilo, 2016c)
CA-SF2(Amilo, 2016a)	CA-SF3(Amilo, 2016d)	CA-TP1(Arain, 2016b)	CA-TP2(Arain, 2016a)	CA-TP3(Arain, 2022b)	CA-TP4(Arain, 2016c)
CA-TPD(Arain, 2022a)	CG-Tch(Nouvellon, 2016)	CH-Aws(Team and Centre, 2022)	CH-Cha(Team and Centre, 2022)	CH-Dav(Team and Centre, 2022)	CH-Fru(Team and Centre, 2022)
CH-Lae(Team and Centre, 2022)	CH-Oe1(Ammann, 2016)	CH-Oe2(Team and Centre, 2022)	CN-Cha(Zhang and Han, 2016)	CN-Cng(Dong, 2016)	CN-Dan(Shi et al., 2016)
CN-Din(Zhou and Yan, 2016)	CN-Du2(Chen, 2016k)	CN-Du3(Shao, 2016b)	CN-HaM(Tang et al., 2016)	CN-Qia(Wang and Fu, 2016)	CN-Sw2(Shao, 2016a)
CZ-BK1(Team and Centre, 2022)	CZ-BK2(Sigut et al., 2016)	CZ-KrP(Team and Centre, 2022)	CZ-Lnz(Team and Centre, 2022)	CZ-RAJ(Team and Centre, 2022)	CZ-Stn(Team and Centre, 2022)



Table 1: **Citation data for the 294 sites used in the X-BASE products.**

CZ-wet(Team and Centre, 2022)	DE-Akm(Team and Centre, 2022)	DE-Geb(Team and Centre, 2022)	DE-Gri(Team and Centre, 2022)	DE-Hai(Team and Centre, 2022)	DE-HoH(Team and Centre, 2022)
DE-Hte(Team and Centre, 2020)	DE-Hzd(Team and Centre, 2022)	DE-Kli(Team and Centre, 2022)	DE-Lkb(Lindauer et al., 2016)	DE-Lnf(Knohl et al., 2016)	DE-Obe(Team and Centre, 2022)
DE-RuR(RI, 2022)	DE-RuS(Team and Centre, 2022)	DE-RuW(Team and Centre, 2022)	DE-Seh(Schneider and Schmidt, 2016)	DE-SfN(Klatt et al., 2016)	DE-Spw(Bernhofer et al., 2016)
DE-Tha(Team and Centre, 2022)	DE-Zrk(Sachs et al., 2016)	DK-Eng(Pilegaard and Ibrom, 2016)	DK-Fou(Olesen, 2016)	DK-Gds(RI, 2022)	DK-Sor(Team and Centre, 2022)
ES-Abr(Team and Centre, 2022)	ES-Agu(Team and Centre, 2022)	ES-Amo(Poveda et al., 2016)	ES-Cnd(Team and Centre, 2022)	ES-LJu(Team and Centre, 2022)	ES-LM1(Team and Centre, 2022)
ES-LM2(Team and Centre, 2022)	ES-LgS(Reverter et al., 2016b)	ES-Ln2(Reverter et al., 2016a)	FI-Hyy(Team and Centre, 2022)	FI-Jok(Lohila et al., 2016)	FI-Ken(Team and Centre, 2022)
FI-Let(Team and Centre, 2022)	FI-Lom(Aurela et al., 2016a)	FI-Qvd(Team and Centre, 2022)	FI-Sii(Team and Centre, 2022)	FI-Sod(Aurela et al., 2016b)	FI-Var(RI, 2022)
FR-Aur(Team and Centre, 2022)	FR-Bil(Team and Centre, 2022)	FR-EM2(RI, 2022)	FR-FBn(Team and Centre, 2022)	FR-Fon(Team and Centre, 2022)	FR-Gri(Team and Centre, 2022)
FR-Hes(Team and Centre, 2022)	FR-LBr(Berbigier and Loustau, 2016)	FR-LGt(RI, 2022)	FR-Lam(Team and Centre, 2022)	FR-Pue(Ourcival, 2016)	FR-Tou(RI, 2022)
GF-Guy(Team and Centre, 2022)	GH-Ank(Valentini et al., 2016b)	GL-Dsk(RI, 2022)	GL-NuF(Hansen, 2016)	GL-ZaF(Lund et al., 2016b)	GL-ZaH(Lund et al., 2016a)
IE-Cra(Team and Centre, 2022)	IL-Yat(Team and Centre, 2022)	IT-BCi(Team and Centre, 2022)	IT-BFt(RI, 2022)	IT-CA1(Sabbatini et al., 2016c)	IT-CA2(Sabbatini et al., 2016a)
IT-CA3(Sabbatini et al., 2016b)	IT-Col(Matteucci, 2016)	IT-Cp2(Team and Centre, 2022)	IT-Cpz(Valentini et al., 2016a)	IT-Isp(Gruening et al., 2016b)	IT-La2(Cescatti et al., 2016)
IT-Lav(Team and Centre, 2022)	IT-Lsn(RI, 2022)	IT-MBo(Team and Centre, 2022)	IT-Noe(Spano et al., 2016)	IT-PT1(Manca and Goded, 2016)	IT-Ren(Team and Centre, 2022)
IT-Ro1(Valentini et al., 2016c)	IT-Ro2(Papale et al., 2016)	IT-SR2(Team and Centre, 2022)	IT-SRo(Gruening et al., 2016a)	IT-Tor(Team and Centre, 2022)	JP-MBF(Kotani, 2016b)



Table 1: Citation data for the 294 sites used in the X-BASE products.

JP-SMF(Kotani, 2016a)	MX-Tes(Yepez and Garatuza, 2021)	MY-PSO(Kosugi and Takanashi, 2016)	NL-Hor(Dolman et al., 2016a)	NL-Loo(Team and Centre, 2020)	PA-SPn(Wolf et al., 2016b)
PA-SPs(Wolf et al., 2016a)	PE-QFR(Griffis and Roman, 2021)	RU-Che(Merbold et al., 2016)	RU-Cok(Dolman et al., 2016b)	RU-Fy2(Team and Centre, 2022)	RU-Fyo(Team and Centre, 2022)
RU-Ha1(Belelli et al., 2016)	SD-Dem(Ardö et al., 2016)	SE-Deg(Team and Centre, 2022)	SE-Htm(Team and Centre, 2022)	SE-Lnn(Team and Centre, 2020)	SE-Nor(Team and Centre, 2022)
SE-Ros(Team and Centre, 2022)	SE-Svb(Team and Centre, 2022)	SJ-Adv(Christensen, 2016)	SJ-Blv(Boike et al., 2016)	SN-Dhr(Tagesson et al., 2016)	US-A32(Billesbach et al., 2022)
US-AR1(Billesbach et al., 2016b)	US-AR2(Billesbach et al., 2016a)	US-ARM(Biraud et al., 2022)	US-ARb(Torn, 2016b)	US-ARc(Torn, 2016a)	US-Atq(Zona and Oechel, 2016a)
US-BZB(Euskirchen, 2022b)	US-BZF(Euskirchen, 2022c)	US-BZS(Euskirchen, 2022d)	US-BZo(Euskirchen, 2022a)	US-Bi1(Rey-Sanchez et al., 2022b)	US-Bi2(Rey-Sanchez et al., 2022a)
US-Blo(Goldstein, 2016)	US-CF1(Huggins, 2021)	US-CF2(Huggins, 2022c)	US-CF3(Huggins, 2022a)	US-CF4(Huggins, 2022b)	US-CRT(Chen and Chu, 2016b)
US-CS1(Desai, 2022a)	US-CS2(Desai, 2022c)	US-CS3(Desai, 2022d)	US-CS4(Desai, 2022b)	US-Cop(Bowling, 2016)	US-EDN(Oikawa, 2021)
US-GBT(Massman, 2016)	US-GLE(Massman, 2022)	US-Goo(Meyers, 2016b)	US-HB1(Forsythe et al., 2021)	US-HWB(Goslee, 2022)	US-Ha1(Munger, 2016)
US-Hn3(Liu et al., 2022)	US-Ho2(Hollinger, 2022)	US-IB2(Matamala, 2016)	US-ICs(Euskirchen et al., 2022a)	US-ICt(Euskirchen et al., 2022b)	US-Ivo(Zona and Oechel, 2016b)
US-Jo2(Vivoni and Perez-Ruiz, 2022)	US-KFS(Brunsell, 2022a)	US-KLS(Brunsell, 2022b)	US-KS1(Drake and Hinkle, 2016a)	US-KS2(Drake and Hinkle, 2016b)	US-KS3(Hinkle, 2022)
US-LWW(Meyers, 2016a)	US-Lin(Fares, 2016)	US-Los(Desai, 2016c)	US-MMS(Novick and Phillips, 2022)	US-MOz(Wood and Gu, 2022)	US-Me1(Law, 2016c)



Table 1: Citation data for the 294 sites used in the X-BASE products.

US-Me2(Law, 2022)	US-Me3(Law, 2016a)	US-Me4(Law, 2016e)	US-Me5(Law, 2016d)	US-Me6(Law, 2016b)	US-Mpj(Litvak, 2021)
US-Myb(Sturtevant et al., 2016)	US-NGB(Torn and Dengel, 2021)	US-NR1(Blanken et al., 2022)	US-Ne1(Suyker, 2022)	US-Ne2(Suyker, 2016b)	US-Ne3(Suyker, 2016a)
US-ONA(Silveira, 2021)	US-ORv(Bohrer, 2021)	US-OWC(Bohrer and Kerns, 2022)	US-Oho(Chen et al., 2016)	US-PFa(Desai, 2016d)	US-Prr(Kobayashi and Suzuki, 2016)
US-Rms(Flerchinger, 2022c)	US-Ro1(Baker et al., 2022)	US-Ro4(Baker and Griffis, 2022a)	US-Ro5(Baker and Griffis, 2021)	US-Ro6(Baker and Griffis, 2022b)	US-Rwe(Flerchinger and Reba, 2022)
US-Rwf(Flerchinger, 2022a)	US-Rws(Flerchinger, 2022b)	US-SRC(Kurc, 2022)	US-SRG(Scott, 2016a)	US-SRM(Scott, 2016b)	US-Sne(Shortt et al., 2022)
US-Snf(Kusak et al., 2022)	US-Sta(Ewers and Pendall, 2016)	US-Syv(Desai, 2016b)	US-Ton(Baldocchi and Ma, 2016)	US-Tw1(Valach et al., 2021)	US-Tw2(Sturtevant et al., 2022)
US-Tw3(Chamberlain et al., 2022)	US-Tw4(Sanchez et al., 2016)	US-Tw5(Valach et al., 2022)	US-Twt(Baldocchi, 2016)	US-UM3(Bohrer, 2022)	US-UMB(Gough et al., 2016)
US-UMd(Gough et al., 2022)	US-Var(Baldocchi et al., 2016)	US-WCr(Desai, 2016a)	US-WPT(Chen and Chu, 2016a)	US-Whs(Scott, 2016d)	US-Wi0(Chen, 2016g)
US-Wi1(Chen, 2016e)	US-Wi2(Chen, 2016j)	US-Wi3(Chen, 2016b)	US-Wi4(Chen, 2016d)	US-Wi5(Chen, 2016a)	US-Wi6(Chen, 2016h)
US-Wi7(Chen, 2016i)	US-Wi8(Chen, 2016c)	US-Wi9(Chen, 2016f)	US-Wjs(Litvak, 2022)	US-Wkg(Scott, 2016c)	US-xBR(Network), 2022)

110 Meteorological data measured at each site consisted of incoming shortwave radiation, air temperature and vapor pressure deficit, of which all data were gap-filled using the Marginal Distribution Sampling method (Reichstein et al., 2005), as well as the computed potential shortwave incoming radiation (top of atmosphere theoretical maximum radiation) for every hour. Carbon dioxide flux data consisted of gap-filled net ecosystem exchange (*NEE*, variable usttar threshold 50th percentile i.e., *NEE_VUT_50*) and the corresponding gross primary productivity (*GPP*, nighttime partitioning method (Reichstein et al.,



115 2005)). Water flux data consisted of evapotranspiration (ET , no energy balance correction) which was converted from the latent energy and transpiration estimates based on the Transpiration Estimation Algorithm (TEA) (Nelson et al., 2018; Nelson, 2021). All data were aggregated to a common hourly time resolution, an overview of which can be found in Table 2.

Table 2: **Fluxes to be predicted and predictor variables used in X-BASE.** The units of the fluxes correspond to the native hourly resolution. Upon temporal aggregation as in some analyses in the presented results, the units may change.

predicted fluxes		
NEE	$\mu\text{mol CO}_2 \cdot \text{m}^{-2} \cdot \text{s}^{-1}$	net ecosystem exchange
GPP	$\mu\text{mol CO}_2 \cdot \text{m}^{-2} \cdot \text{s}^{-1}$	gross primary productivity
ET	$\text{mm} \cdot \text{hr}^{-1}$	evapotranspiration
ET_T	$\text{mm} \cdot \text{hr}^{-1}$	transpiration

predictor variables		
air temperature		$^{\circ}\text{C}$
vapor pressure deficit		hPa
incoming shortwave radiation		$\text{W} \cdot \text{m}^{-2}$
potential incoming shortwave radiation		$\text{W} \cdot \text{m}^{-2}$
derivative of daily pot. incoming shortwave radiation		$\text{W} \cdot \text{m}^{-2} \cdot \text{d}^{-1}$
derivative of hourly pot. incoming shortwave radiation		$\text{W} \cdot \text{m}^{-2} \cdot \text{hr}^{-1}$
daytime land surface temperature from MODIS TERRA		kelvin
nighttime land surface temperature from MODIS TERRA		kelvin
enhanced vegetation index		-
near-infrared reflectance of vegetation		-
normalized difference water index		-
plant functional type		-

120 Data from the EC dataset that ultimately were used for training the models varied between ~12-14 million site-hours depending on the target variable (i.e. GPP , NEE , ET , or ET_T). Training of the machine learning algorithms was only conducted on hours where all input variables passed quality control. The quality control procedure consisted of two levels, with the first being each hour must have at least one value of good quality measured or gap-filled with confidence (i.e. at least one half hour was either 0 or 1 based on the OneFLUX _QC flags). Second, a set of consistency tests were performed on each used variable to check the consistency both among variables and across sites. As the consistency flags were based on daily aggregates of the meteorological and flux data, entire days were removed if the test indicated inconsistencies among related variables. The



125 consistency flag also checked the relationship between variables across sites, ensuring that the relationships found across the data are coherent. A detailed explanation of these consistency flags can be found in Jung et al. (2023).

2.2 Global Meteorology

For the generation of global flux maps we used hourly meteorological data from ERA5 global reanalysis products at 0.25° (Hersbach et al., 2020). Variables included air temperature at 2m height, incoming shortwave radiation at the surface, as well 130 as vapour pressure deficit (computed from relative humidity, air temperature, and surface pressure). Units were converted to correspond to the site level measurements which were used for training the machine learning model, and the data were re-gridded to a 0.05° resolution using bilinear interpolation for every hour.

2.3 Satellite Earth Observation

The X-BASE products are based on measurements of the MODerate Imaging Spectroradiometer (MODIS) of surface reflectance and land surface temperature from collection v006 at daily resolution. Missing records were gap-filled consistently 135 in both the average time series per EC station and in the global gridded data following the procedures of the FluxnetEO data version 2 (Walther and Besnard et al., 2022; Walther, 2023).

2.3.1 Spectral vegetation indices

At site level we used surface reflectance in the first seven MODIS spectral bands from the MCD43A4 v006 reflectance data 140 set (500 m and daily, where each daily value is inverted from all valid observations within a 16-day window (Schaaf and Wang, 2015b)). The spectral vegetation indices computed from the reflectance data were the enhanced vegetation index (EVI) (Huete et al., 2002), the spectral reflectance of vegetation in the near-infrared (NIRv) (Badgley et al., 2017), and the normalized difference water index (NDWI) with MODIS band 7 as reference (Gao, 1996). We followed the procedure of the FluxnetEO data sets version 2 (Walther and Besnard et al., 2022) for data acquisition from Google Earth Engine for all pixels in a cutout 145 of $4 \times 4 \text{ km}^2$ around each EC station, as well as for quality checks in terms of snow cover, land cover, index values outside the defined ranges, and outliers. An iterative approach then determined both, the strictness of the inversion quality of the bidirectional reflectance distribution function (BRDF, based on the MCD43A2 data, (Schaaf and Wang, 2015a)) and the set of pixels in a cutout that shall represent a given EC station. Supporting information section A1 outlines all technical details of the dynamic procedure.

150 Global data of BRDF-corrected surface reflectance stem from the MCD43C4 v006 data (Schaaf and Wang, 2015b), available in a climate modelling grid of 0.05° with the same temporal sampling and subject to the same removal of snow and water pixels and outlier values like at site level. The BRDF quality control of the global data followed the same dynamic approach (see supporting information A1), which maximized data availability especially in tropical regions.



2.3.2 Land surface temperature

155 Satellite observations of land surface temperature (LST) were based on the MODIS v006 TERRA observations which are available every day at 1 km resolution (Wan et al., 2015). We selected the 1 km² pixel containing a specific tower and treated the two MODIS LST data streams as independent predictor variables which represent clear-sky LST at a specific time of the day (namely around 10.30 AM and PM local time). Quality checks and gap-filling followed the procedure described in FluxnetEO version 2 (Walther and Besnard et al., 2022).

160 For the global spatialization of the flux estimates we relied on climate modelling grid LST from the MODIS TERRA data sets (Wan et al., 2015) and apply consistent quality control and imputation of missing values like at site-level.

2.3.3 Land cover

Land cover information used the IGBP global vegetation classification. Site level classification was as reported by the principal investigators. Global data were based on the yearly-resolved MODIS MCD12Q1 v006 product (Friedl and Sulla-Menashe, 165 2019). In order to ease the transition between site and global land cover classifications, an intermediate classification scheme was utilized which translated each classification into characteristics (e.g. trees, crops, needleleaf, deciduous, etc...) based on whether the classification has (value=1.0), might have (value=0.5), does not have (value=0.0) a specific feature, or is unknown (value=-1.0). A full description of this intermediate classification system can be found in supplementary section A2.

2.4 Machine Learning Method

170 All X-BASE products are based on gradient boosted regression trees using the XGBoost library (Chen and Guestrin, 2016). XGBoost is known as a robust algorithm that is able to handle a variety of variable types (numeric, boolean, categorical). Training was conducted using a two-thirds training sub-sampling ratio and a 0.05 learning rate. Boosting was stopped when no model improvement (based on mean squared error of validation data) was observed for ten consecutive rounds, and the best 175 performing model was stored to generate predictions. In all cases, the model reached the stopping criteria relatively quickly, with the final number of boosting rounds between 80-230, depending on the flux.

2.5 Cross-validation

All cross-validation was performed using a 10 fold, leave-site-fold-out scheme, where each fold was constructed by randomly assigning each site to a fold. For each round of cross-validation, eight folds were used for training, one for validation and the remaining one as the test fold for which the actual predictions were made. The leave-site-fold-out scheme ensures that no data 180 from the sites in the test fold were ever seen by the algorithm during training, and in turn iterated such that each site was in the test set once. As eddy covariance sites are sometimes clustered in the same location (e.g. as different treatments) and can therefore be both physically closely located and not truly independent, sites are assigned to the same fold if they are less than 0.05° apart to reduce over-fitting. We evaluate the accuracy of the cross-validation models by computing the Nash-Sutcliffe modeling efficiency (NSE, Nash and Sutcliffe (1970)), where a negative NSE indicates a model accuracy that is worse than a



185 mean prediction, while a value close to one indicates high model accuracy. We compute the NSE for each site and for a range of temporal scales from hourly to inter-annual.

2.6 Up-scaling

190 The final step to train a model to use in the final global prediction step was identical to the training in the cross-validation, with the exception that, because no test fold was required, we used nine of the ten folds for the training and validation was done on the remaining fold. The final trained models (one trained model for each target flux) were then used to predict fluxes at the global scales using the associated globally gridded input variables that correspond to those used at site level, as outlined in Table 2.

2.7 Previous FLUXCOM and independent global flux estimates

195 We compare X-BASE with up-scaling results from FLUXCOM (Jung et al., 2019, 2020). As mentioned earlier, FLUXCOM comprised an ensemble of up-scaling experiments that differed in the choice of machine learning method, meteorological forcing data, and which were summarized in two groups of set-ups that shared the same predictor variables and spatiotemporal resolution: The “remote-sensing-only” set-up (RS) mostly used spaceborne observations of MODIS as explanatory variables and produced flux estimates every 8 days at 0.083° resolution, while the ‘remote-sensing plus meteorology set-up’ (RS+METEO) produced daily flux estimates at half degree resolution from meteorological predictor variables and an average seasonal cycle 200 of satellite observations (Tramontana et al., 2016; Jung et al., 2019, 2020). Comparisons to FLUXCOM RS+METEO datasets always refer to the ensemble over multiple machine learning methods for all realizations driven by the ERA5 meteorology (Hersbach et al., 2020). RS+METEO uses average seasonal cycles of MODIS v005 observations. For the FLUXCOM RS set-up we use the ensemble over all machine learning methods. Please note that both the previous RS runs and the X-BASE runs presented here are driven by data from MODIS v006, but the processing has changed in some aspects such as quality control 205 and gap-filling.

For evaluating X-BASE *NEE* globally, in particular its seasonal cycle and for different regions, we used two different atmospheric inversion model products: the Orbiting Carbon Observatory-2 (OCO-2) v10 model intercomparison project (Byrne et al., 2023) and the CarboScope inversion (Rödenbeck et al., 2018) version s99oc_v2022 (Roedenbeck and Heimann, 2022). Estimates from the OCO-2 came from the the LNGLIS experiment which combines satellite-based column-averaged CO_2 210 (XCO2) retrievals and in-situ CO_2 measurements as observational constraints in the assimilation, and consists of 13 different ensemble members covering the period 2015-2020 with a monthly frequency and 1° spatial resolution (https://gml.noaa.gov/ccgg/OCO2_v10mip/index.php). The CarboScope product consisted of a single inversion output at the same spatial resolution as OCO-2, but a longer temporal period from 2001 to 2020. In each case, as the inversion products estimate net biome exchange, we subtracted from the inversions data fire emissions as estimated by the Global Fire Emissions Database, Version 4.1 215 (Randerson et al., 2017).

We compared temporal patterns of X-BASE *GPP* with the patterns in global retrievals of sun-induced chlorophyll fluorescence (SIF) from the Sentinel-5P TROPOMI instrument (Köhler et al., 2018), which under most conditions approximate the



variability in GPP . For the comparison we used estimates of daily mean SIF applying a correction factor to instantaneous observations (Zhang et al., 2018) and averaged both X-BASE GPP and TROPOMI SIF to a temporal resolution of 16 days
220 and 0.5° spatial grids for the common period 04/2018-12/2020.

X-BASE ET and ET_T were cross-compared with transpiration estimates from the Global Land Evaporation Amsterdam Model (GLEAM) v3.6a (Martens et al., 2017; Miralles et al., 2011). GLEAM also utilizes satellite and reanalysis data sets but in a more physically constrained way, relying on semi-empirical models such as the Priestley and Taylor (Priestley and Taylor, 1972) and Gash models (Gash, 1979). Further comparisons were made to precipitation data from GPCC (Schneider
225 et al., 2022).

3 Results

3.1 Cross-validation and data space

One important innovation in FLUXCOM-X compared to the previous FLUXCOM ensemble was the training data base, which
230 was larger due to an increase in both number of sites and years. Furthermore, the EC methodology has changed considerably in many aspects ranging from collection and processing to quality filtering in the last 15 years. We show here one illustrative example of the changes in the environmental space that is represented in the training samples for daily NEE : between daily VPD and daily incoming shortwave radiation the distribution of training samples was considerably broader in X-BASE compared to the RS+METEO ensemble (Fig. 1). Furthermore, the number of unique sites contributing to a certain VPD-radiation bin has increased (Fig. B1), i.e. the number of ecosystems sampled in each climatic condition has also increased. The increases
235 were seen particularly at the margins of the distribution, i.e. for days with high VPD along the full radiation spectrum, and vice versa for days with high radiation conditions along the full VPD spectrum. Remarkably, the number of sites contributing training samples for high VPD *and* high radiation were observed much more frequently (Fig. 1) and at more sites (Fig. B1) compared to RS+METEO - providing more and more varied information for dry conditions.

The results from the ten-fold cross validation showed an overall high performance with most fluxes and scales of variability
240 having an NSE above 0.6 (Fig. 2). In terms of scales of variability across all fluxes, the monthly mean diel cycle (“diel”) and the daily median seasonal cycle (“seasonal”) were very regular patterns that the trained models reproduced best. Also, among-site changes (“spatial”, except for NEE) and monthly aggregated fluxes (“monthly”) were reliably predicted. Deviations from the median daily seasonality (“anom”) were only moderately reliable with NSE between 0.25 and 0.5. The XGBoost models did not succeed in accurately reproducing inter-annual changes (“i.a.v.”) of all fluxes and between-site patterns in NEE . Consistently
245 across all scales, the net fluxes which are directly calculated (i.e., ET and even more so NEE) showed lower performance than their respective modelled gross fluxes (i.e., GPP and ET_T). Note that the cross validation results from Fig. 2 cannot be quantitatively compared to previous cross validation results in FLUXCOM as the training data are not the same. However, qualitatively the accuracy gradient among fluxes as well as along scales of variability corresponded to patterns identified in FLUXCOM and in comparable empirical modeling activities (Jung et al., 2011; Tramontana et al., 2016; Virkkala et al., 2021;
250 Dannenberg et al., 2023).

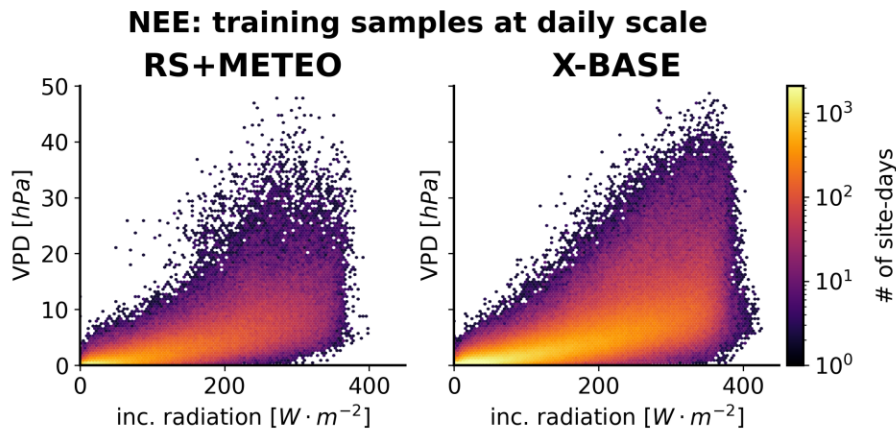


Figure 1. Cross-validation sampling in meteorological space: Number of site-days contributing to sampling for *NEE* for the previous FLUXCOM RS+METEO ensemble (left) compared to the sampling of FLUXCOM-X-BASE (right) in environmental space of daily aggregated incoming shortwave radiation and VPD. Color corresponds to number of site days per bin in log scale. Only bins with at least twenty site-days are shown.

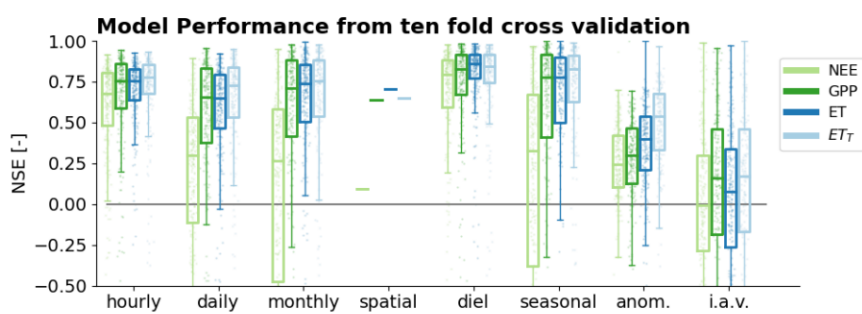


Figure 2. FLUXCOM-X-BASE site-level accuracy of predicted fluxes in 10-fold leave-site fold-out cross-validation in terms of NSE computed per site for a range of scales of variability. Scales of variability include the hourly timescale (“hourly”), daily (“daily”) and monthly (“monthly”) aggregated fluxes, as well as between-site changes (“spatial”), monthly mean diel cycle (“diel”), daily median seasonal cycle (“seasonal”), deviations from the median daily seasonality (“anom.”), and inter-annual variability (“i.a.v.”). Boxes denote the range from the 25th to the 75th percentile of sites, whiskers extend 1.5 times the interquartile range from the 25th and 75th percentile of NSE across sites.

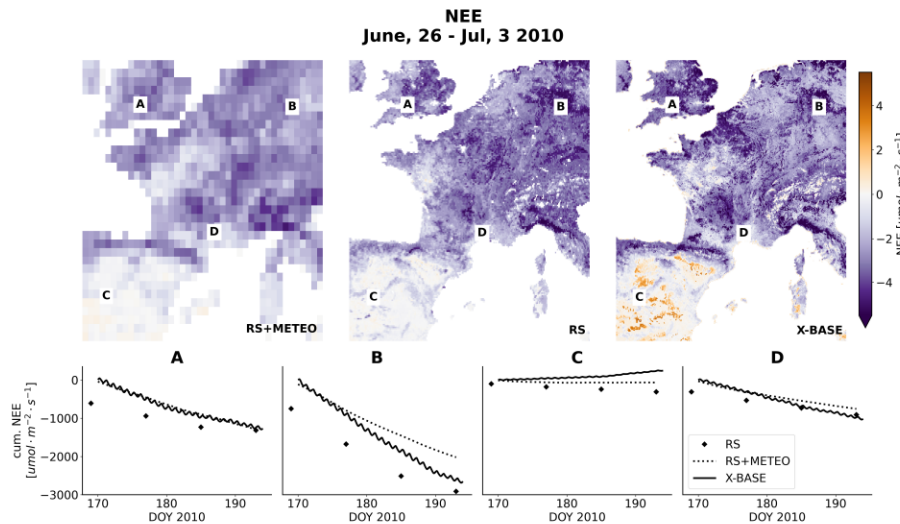


Figure 3. Resolution improvements for the X-BASE products compared to RS and RS+METEO: Average NEE for an 8-day period in Europe in 2010 as estimated from the RS, RS+METEO and X-BASE set-ups (top panel), as well as snapshots of temporal trajectories of NEE in pixels closest to selected EC station locations (A:UK-Tad, B: DE-Hai, C: ES-LM1, D: FR-Pue). Negative values of NEE denote a CO_2 flux from the atmosphere to the land.

3.2 Global flux estimates

One asset of FLUXCOM-X is flexibility in the spatiotemporal resolution of the flux estimates. We are producing X-BASE products at 0.05° spatial and hourly temporal resolution globally. Figure 3 illustrates the increase in spatial and temporal detail in X-BASE compared to RS (0.083°, 8-daily) and RS+METEO (0.5°, daily) using the example of NEE .

255 3.2.1 Net Ecosystem Exchange (NEE)

The X-BASE product estimates the global terrestrial NEE to be $-5.75 \pm 0.33 \text{ PgC yr}^{-1}$ (2001-2020), with strong CO_2 uptake hotspots in the tropical regions, and temperate regions of North America and Europe (Fig. 4). In contrast to both RS and RS+METEO, India and some regions in central Sahel show prominent patterns of a mean CO_2 flux from the ecosystems to the atmosphere in X-BASE, corresponding mostly to crop designated areas (Fig. B2). However, comparing X-BASE 260 global terrestrial NEE to the inversion estimates (corrected for fire emissions based on GFED 4.1 (Randerson et al., 2017)) over the common period (2015-2020) shows agreement of X-BASE ($-5.63 \text{ PgC yr}^{-1}$) with OCO-2 ($-4.12 \text{ PgC yr}^{-1}$) and CarboScope ($-3.46 \text{ PgC yr}^{-1}$).

Comparison with OCO-2 and CarboScope inversions also indicates a substantial improvement of the global mean seasonal cycle of NEE (Fig. 5) in X-BASE compared to RS and RS+METEO. The systematic bias present in RS and RS+METEO has 265 essentially disappeared in X-BASE. The shape, and in particular the amplitude, of the global NEE seasonal cycle of X-BASE

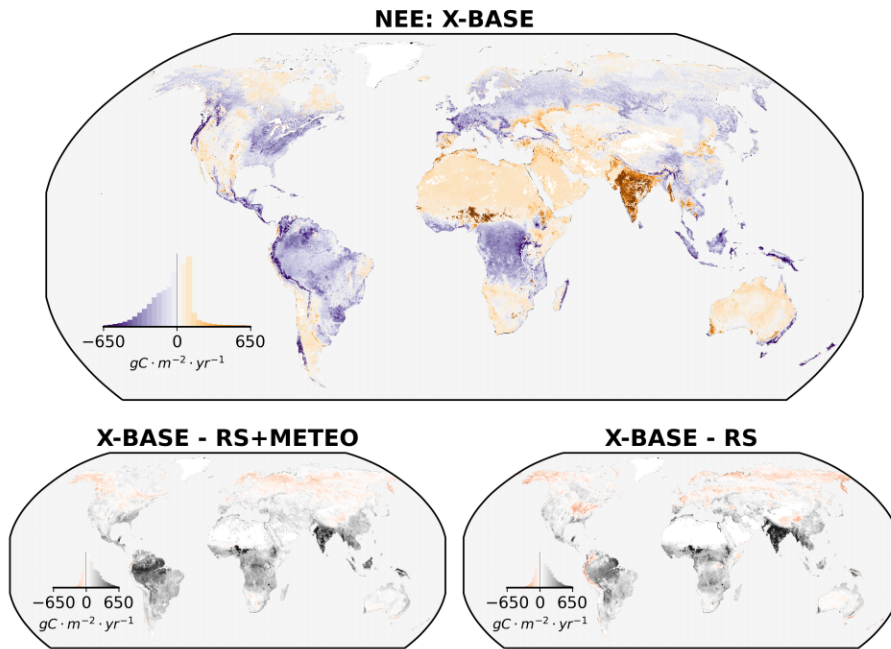


Figure 4. Comparison of annually integrated NEE from X-BASE, RS+METEO with ERA5 forcing and RS averaged over the period 2001-2020. The difference maps show the difference of the averages over 2001-2020.

is more consistent with the inversions. The larger and more realistic seasonal cycle amplitude of global NEE in X-BASE originates primarily from improved and increased amplitudes in boreal regions. Interestingly, X-BASE suggests slightly larger NEE seasonal cycle amplitudes in temperate regions compared to the inversions. In seasonally dry regions, the timing of maximum uptake is consistent between X-BASE and inversions, while the peak of maximum net release is larger and delayed 270 in the inversions. In Australia, the peak of CO_2 release to the atmosphere at the end of the year present in both inversions is not evident in X-BASE, which instead shows a relatively consistent CO_2 flux to the atmosphere throughout the year. In tropical regions, the patterns of seasonal variations are qualitatively consistent between X-BASE and the previous RS and RS+METEO products. The seasonal patterns in tropical regions are relatively weak overall and seem inconsistent both between the inversions and X-BASE as well as among the inversions.

275 As seen in Figure 5, the X-BASE product shows the same large underestimation of globally integrated NEE inter-annual variance as the previous RS and RS+METEO products. In terms of temporal trends, the X-BASE products show almost no change in annual NEE in time, which is in contrast to the RS+METEO (slight positive trend) and RS (slight negative trend) and more consistent with the CarboScope inversions (Table B2). However, as inter-annual variability was poorly reproduced even in the cross validation (Fig. 2), trends in the X-BASE products should be taken with caution and interpreted with careful 280 scrutiny.

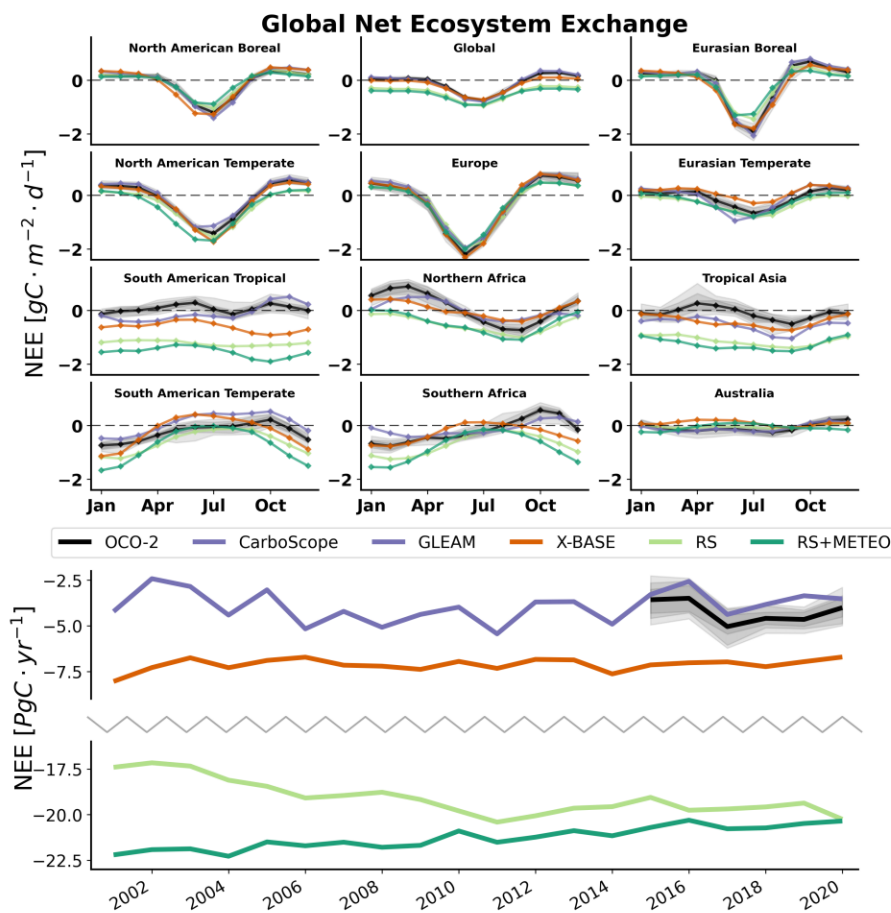


Figure 5. Seasonal and inter-annual variability of global NEE. Comparison of mean seasonal cycles (calculated over the common time period, 2015-2020) and inter-annual variability (2001-2020) of NEE estimated from CARBOSCOPE and OCO2 inversions as well as FLUXOM-X-BASE and FLUXCOM RS+METEO and RS outputs. All products were integrated with a common mask that removes sparsely vegetated arid regions not predicted by RS and RS+METEO.

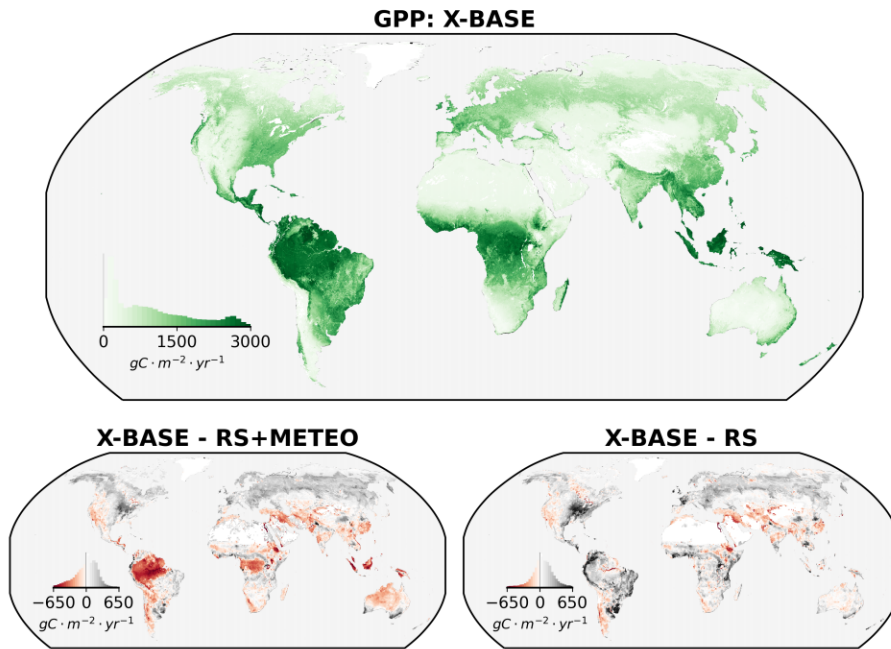


Figure 6. Comparison of annually integrated *GPP* from X-BASE, RS+METEO with ERA5 forcing and RS averaged over the period 2001-2020. The difference maps show the difference of the averages over 2001-2020.

3.2.2 Gross Primary Productivity (GPP)

X-BASE estimates the globally integrated *GPP* at $124.7 \pm 2.1 \text{ PgC} \cdot \text{yr}^{-1}$ on average in the time period 2001-2020. Globally integrated *GPP* over vegetated areas (RS and RS+METEO do not have estimates for non-vegetated areas) was approximately equal for X-BASE ($121.9 \pm 2.1 \text{ PgC} \cdot \text{yr}^{-1}$) and RS+METEO ($121.6 \pm 0.4 \text{ PgC} \cdot \text{yr}^{-1}$) but considerably higher than RS 285 (113.2 $\pm 1.8 \text{ PgC} \cdot \text{yr}^{-1}$) over the same period. In terms of regional patterns, X-BASE *GPP* consistently exceeds both RS+METEO and RS in temperate, boreal, and most subtropical ecosystems, but is lower in sparsely vegetated (semi-)arid regions like southwestern North America as well as southeast Asian croplands (Fig. 6). This qualitatively consistent pattern is only broken in the humid tropics, where X-BASE *GPP* is higher than RS, but lower than RS+METEO.

Comparing the estimated trend over the last two decades, X-BASE *GPP* has a clear increasing linear trend of $0.34 \text{ PgC} \cdot \text{yr}^{-2}$ 290 which is slightly higher than the trend in RS ($0.25 \text{ PgC} \cdot \text{yr}^{-2}$, Table B2). In contrast, the RS+METEO product shows nearly no trend in annual *GPP*. The increases in both the X-BASE and RS products may be related to increases in surface greenness coming from variability in the remote sensing forcing data which are inter-annually dynamic in both products, whereas the remote sensing data were not inter-annually dynamic in the RS+METEO product which instead used only the mean seasonal cycle of the remote sensing data. The magnitude of between-year changes in globally integrated X-BASE *GPP* 295 is $0.575 \text{ PgC} \cdot \text{yr}^{-1}$ over the years 2001-2020, which is about twice as large as RS+METEO ($0.248 \text{ PgC} \cdot \text{yr}^{-1}$), but only half the magnitude estimates in the RS set-up ($1.02 \text{ PgC} \cdot \text{yr}^{-1}$, Table B2).



We further compared the temporal trajectory in *GPP* estimates against TROPOMI SIF as an independent proxy for *GPP* dynamics (Fig. 7) at a temporal resolution of 16 days. The temporal variability of X-BASE *GPP* strongly agrees with that in TROPOMI SIF, with Squared Spearman correlation values (denoted as R^2) of the time series above 0.85 across most of the 300 vegetated land surface (Fig. 7 top left). The only exceptions are regions with no or very small variability in both *GPP* and SIF such as in either evergreen tropical ecosystems in South America, Africa and southeast Asia, or sparsely to non-vegetated areas due to aridity (e.g. Mexican, and African deserts) or cold conditions (e.g. Canadian and Siberian subpolar regions). In inner 310 Australia, despite being sparsely vegetated, variability between years is expected in *GPP* due to precipitation increases during La Nina years, which is however not reflected in the squared correlations. R^2 for the deviations from the average seasonality 320 (again computed with a temporal resolution of 16 days) show the same qualitative spatial patterns (Fig. 7 top right), but are overall lower with R^2 values between 0.55 and 0.8. Anomalies of X-BASE *GPP* and SIF agree best in eastern European temperate forests as well as grassy and shrub ecosystems in eastern South America.

Comparison of the level of agreement of SIF and X-BASE with that of SIF and RS and RS+METEO, respectively, illustrates 330 that X-BASE and RS *GPP* estimates have comparable consistency both for the time series (global area weighted mean R^2 values of 0.72 and 0.73, respectively) and anomalies (global mean R^2 values of 0.64 and 0.66, respectively). In contrast, the R^2 between RS+METEO and SIF is lower in both cases (R^2 values of 0.66 for the time series and 0.58 for anomalies). X-BASE 340 *GPP* shows a higher agreement with SIF than RS both in terms of the actual trajectory and anomalies in evergreen tropical forests with no or only a very short dry season in the Amazon and Africa, as well as in fully humid parts of southeast Asia (Fig. 350 7 middle panel). Improvements in X-BASE *GPP* compared to RS are also consistent in the very continental and polar tundra areas in eastern Siberia, northern Canada and Alaska. Conversely, in arid steppe climates globally, X-BASE *GPP* variability 360 agrees less with SIF than does RS *GPP*. X-BASE *GPP* variability is consistently and widespread much more similar to the variability in TROPOMI SIF than RS+METEO *GPP*. Increases in R^2 for X-BASE compared to RS+METEO are most 370 pronounced in arid to semi-arid ecosystems (large parts of the Caatinga and Gran Chaco regions on South America, steppe regions in Mexico, southern and eastern Africa, Australia and central Siberia) as well as in global crop regions, especially for 380 the deviations from the seasonality (albeit the magnitude of R^2 change is quite variable between regions, Fig. 7 bottom).

3.2.3 Water Vapor Fluxes

Globally integrated *ET* amounts to $74.7 \times 10^3 \pm 0.9 \times 10^3 \text{ km}^3 \cdot \text{yr}^{-1}$ for 2001-2020 (Table B1) for X-BASE, with the highest 390 rates in the tropics (Fig. 8). Comparing global totals for vegetated areas only (where all products give outputs) shows similar values for X-BASE ($68.9 \times 10^3 \pm 0.9 \times 10^3 \text{ km}^3 \cdot \text{yr}^{-1}$), GLEAM ($70.9 \times 10^3 \pm 0.9 \times 10^3 \text{ km}^3 \cdot \text{yr}^{-1}$) and RS+METEO ($68.3 \times 10^3 \pm 0.3 \times 10^3 \text{ km}^3 \cdot \text{yr}^{-1}$) *ET* estimates, while the RS *ET* is more than 11% higher ($78.5 \times 10^3 \pm 0.5 \times 10^3 \text{ km}^3 \cdot \text{yr}^{-1}$, Table B1). 400 Particularly in evergreen tropical ecosystems, X-BASE estimates a considerably lower *ET* than both GLEAM, RS+METEO, and RS (Fig. 8). Furthermore, in the temperate and high latitudes of the northern hemisphere, annually integrated X-BASE *ET* is consistently lower than the other estimates, though the magnitude of the bias is smaller than in the tropical regions. 410 The pattern is only reversed with higher X-BASE *ET* in the semi-arid and arid ecosystems of the lower and middle latitudes, especially with respect to annual *ET* in RS+METEO and GLEAM.

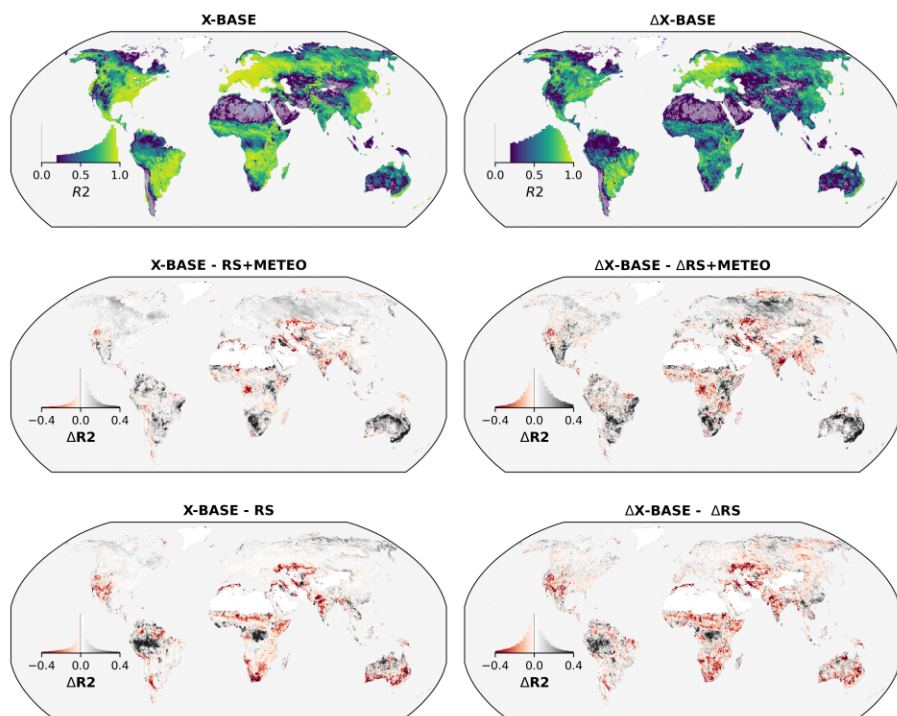


Figure 7. Similarity of temporal patterns between GPP estimates and TROPOMI SIF observations: R^2 (computed as the square of the Spearman correlation) between X-BASE GPP and TROPOMI SIF (Köhler et al., 2018) for the actual time series at a temporal resolution of 16 days (top left) and anomalies from the median seasonality in both variables (top right). The middle and the bottom panels relate the agreement between X-BASE GPP and TROPOMI SIF to the agreement between FLUXCOM GPP and TROPOMI SIF, where the middle panel refers to TROPOMI SIF and GPP from the RS+METEO set-up, and the bottom panel to the RS set-up. All comparisons are done for time series with a resolution of 16 days for the common time period 04/2018 to 12/2020. SIF observations have been applied a correction factor to estimate daily average SIF before aggregation. Semi-transparent areas mark pixels in which the correlation of at least one of the data sets is negative.



Comparison to precipitation estimates shows that X-BASE ET greatly exceeds precipitation inputs over large areas, indicating a strong overestimation of X-BASE ET in many arid regions with sparse vegetation (e.g. the Sahara region, Fig. B3). While transport of water both laterally and from deeper groundwater could cause ET to exceed precipitation inputs in some areas, the extent of area where ET exceeds precipitation (e.g. the entire Sahara region) and the magnitude of the excess ET (over three times precipitation inputs) indicates a major bias in these areas and is likely due to a lack of EC data in similar ecosystems. As a rough estimate, constraining the X-BASE estimates with precipitation (see supplement section B5) suggests about $4.6 \times 10^3 \text{ km}^3 \cdot \text{yr}^{-1}$ of water is overestimated globally.

The globally integrated ET_T amounts to $42.6 \times 10^3 \pm 1.0 \times 10^3 \text{ km}^3 \cdot \text{yr}^{-1}$ (2001-2020) in X-BASE, resulting in an average ratio of transpiration to total evaporation of $57.0\% \pm 0.6\%$ (Table B1). In contrast to ET , the ET_T estimates from X-BASE do not commonly exceed precipitation estimates (Fig. B3), which could indicate that because the water vapor flux is more tightly coupled with vegetation, the model is able to distinguish that no vegetation corresponds with no transpiration, which is not generally the case for non-transpiration evaporation. The RS and RS+METEO products did not produce ET_T estimates, so the comparison is limited to GLEAM ($50.7 \times 10^3 \pm 0.6 \times 10^3 \text{ km}^3 \cdot \text{yr}^{-1}$), which estimates ET_T on average 17% higher than X-BASE, with strong contributions from the evergreen tropics. Only in single semi-arid regions, such as northernmost Sahel as well as large parts of the South American Caatinga and Chaco regions is this pattern reversed (Fig. 8).

Spatially, X-BASE-estimated ET_T/ET exceeds 50% in the majority of areas, with the highest values seen in the higher latitude regions of Europe and Asia, as well as in subtropical ecosystems (Fig. 8). Arid regions with sparse vegetation show the lowest ET_T/ET overall, with values generally below 20%. With $71.4\% \pm 0.6\%$ over global vegetated surfaces, GLEAM attributes about 10% more of its ET to ET_T than does X-BASE (Table B1). Regionally, this difference can even reach up to 40%, with the only exception being boreal forests and very dry ecosystems in the Sahel, the Arabian Peninsula and central Asia (Fig. 8).

Trends in ET , ET_T and ET_T/ET are positive and exceed the trends seen in all other estimates over the years 2001-2020. Conversely, the magnitude of inter-annual changes in X-BASE ET , ET_T , and ET_T/ET is mostly less than half than the variability in GLEAM (Table B2). Low inter-annual changes are common to the RS and RS+METEO ET as well.

Figure 9 shows the temporal correlation at 16-daily temporal scale using GLEAM as a reference, showing overall high values of squared correlation between X-BASE and GLEAM ET and ET_T (top and bottom left). Notable exceptions with low correlations are areas with low variability in ET such as the arc of deforestation, very dry areas, and tropical evergreen ecosystems in Africa. Compared to RS+METEO and RS (middle panels left column in Fig. 9), X-BASE ET temporal patterns are more similar to GLEAM ET in many areas, and especially so in areas north of the arc of deforestation and parts of tropical evergreen areas in central Africa and southeast Asia. Conversely, X-BASE ET agrees less well with GLEAM than RS or RS+METEO in the arc of deforestation itself, the eastern parts of the Amazon basin, as well as dry areas. The deviations from the mean annual cycle in ET and ET_T (right column) show overall lower correlations than the actual time series, with the highest agreement between GLEAM and X-BASE in large parts of the Amazon forest and central European ecosystems. X-BASE ET anomalies are much more strongly correlated with GLEAM ET than either RS or RS+METEO everywhere except for most (semi-)arid regions.

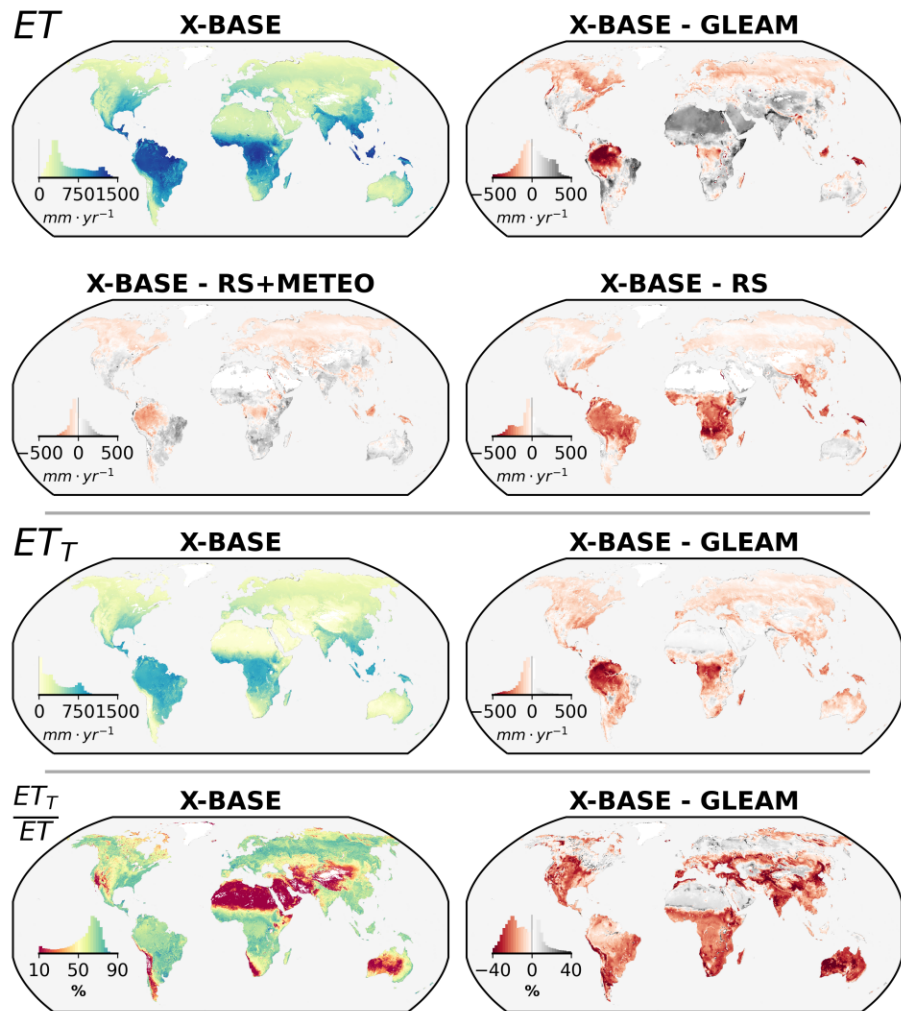


Figure 8. Comparison of evaporative flux estimates ET , ET_T and ET_T/ET from X-BASE and its difference with RS, RS+METEO, and GLEAM. ET_T is compared in the case of GLEAM, but is unavailable in the previous FLUXCOM ensembles.

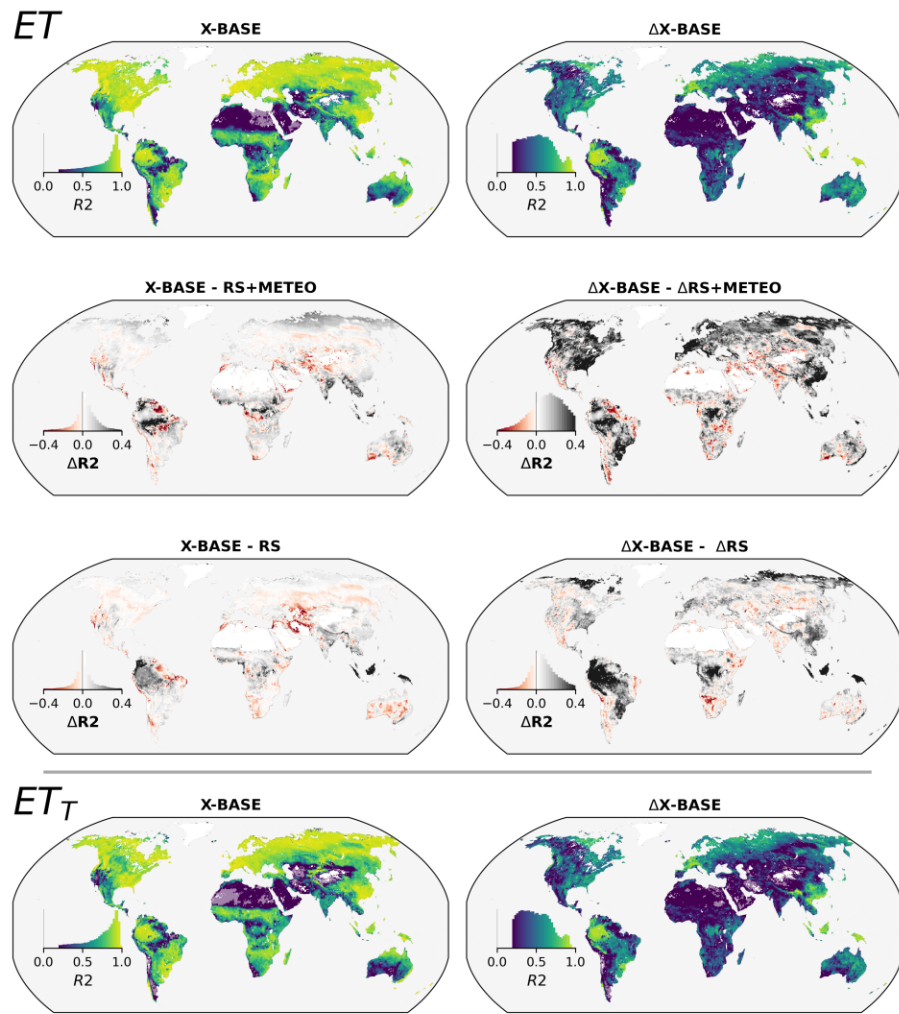


Figure 9. R^2 (computed as the square of the Pearson correlation) between X-BASE ET and GLEAM ET for the actual time series (left column) and anomalies from the median seasonality (right column). The middle panels compare the agreement between X-BASE ET and GLEAM ET to the agreement between FLUXCOM ET and GLEAM ET . The bottom panel shows the squared correlations between X-BASE and GLEAM ET_T , but no comparisons to FLUXCOM because FLUXCOM did not include ET_T . All comparisons are done for time series with a resolution of 16 days and 0.05 degrees for the years 2001-2020. Semi-transparent areas mark pixels in which the correlation of at least one of the data sets is negative.



4 Discussion

4.1 Higher consistency of *NEE* with atmospheric carbon cycle constraints

Although FLUXCOM-X follows the same fundamental approach as FLUXCOM, we find a substantial improvement of the magnitude of the annually integrated *NEE* of FLUXCOM-X-BASE over previous FLUXCOM products (Jung et al., 2020)

370 when compared to independent estimates from atmospheric inversions. The mean global X-BASE *NEE* of $-5.75 \text{ PgC} \cdot \text{yr}^{-1}$ is slightly smaller than the inferred *NEE* of $-3.92 \text{ PgC} \cdot \text{yr}^{-1}$ (corrected for fire emissions based on GFED 4.1) from CarboScope. The remaining difference could easily be explained by carbon sources such as aquatic evasion and volatile organic compounds that are included in the atmospherically based estimate but not in eddy-covariance based FLUXCOM (see Jung et al. (2020) and Zscheischler et al. (2017) for further discussion).

375 The improved global *NEE* of FLUXCOM-X-BASE originates most likely from enhanced quality of eddy covariance measurements in the training. Previous up-scaling-based *NEE* products of (Jung et al., 2011, 2020; Bodesheim et al., 2018) - all based on the La Thuile FLUXNET dataset but varying with respect to machine learning methods, predictor variables, and temporal resolution - consistently estimated a nearly three-fold larger global terrestrial carbon uptake compared to X-BASE. As discussed and speculated in Jung et al. (2020), La Thuile likely contained biased *NEE* measurements, in particular for 380 some tropical sites (Fu et al., 2018), and together with the sparsity of data in the tropics, these biases were propagated to unrealistic tropical and global *NEE* estimates. The fact that we can now reconcile bottom-up global eddy-covariance-based *NEE* and estimates from top-down atmospheric inversions is a major achievement of the FLUXNET community. For context: 1 $\text{PgC} \cdot \text{yr}^{-1}$ over the global vegetated area ($145 \times 10^6 \text{ km}^2$) corresponds to $\sim 7 \text{ gC} \cdot \text{m}^2 \cdot \text{yr}^{-1}$, which marks a challenge for achieving such accuracy of mean *NEE* at any one flux tower site. The lesson learned here emphasizes once more that it is 385 crucial to control for and minimize systematic biases of in-situ eddy covariance measurements (Moncrieff et al., 1996).

The improved seasonality of X-BASE *NEE*, in particular for boreal regions, likely also results from enhanced information in the training data due to the hourly resolution. Similar improvements were observed in Bodesheim et al. (2018) who extended RS+METEO by training on half-hourly flux observations. The hourly resolution improves the seasonal high-latitude *NEE* likely due to better capturing the responses to light when daylength varies strongly.

390 4.2 New opportunities by X-BASE products

The improvements of *NEE* make X-BASE attractive as a data-driven biogenic prior for atmospheric inversions (Munassar et al., 2022). Moreover, its hourly resolution facilitates better integration in inversion systems due to the accounting of diurnal flux and atmospheric transport variations, while its high spatial variations can provide patterns of flux variations that cannot be resolved by atmospheric constraints alone.

395 For the first time, X-BASE includes a global data-driven product of ecosystem transpiration. The estimated global ET_T/ET ratio of 57% is consistent with independent top-down assessments from isotope base methods (Good et al., 2015; Coenders-Gerrits et al., 2014) and past up-scaling estimates (Wei et al., 2017; Schlesinger and Jasechko, 2014). The spatially and temporally high resolution data-driven X-BASE ET_T product provides a valuable complementary perspective to simulations from



process-based land surface models, which show large disagreements and often indicate global ET_T/ET below 50% (Berg 400 and Sheffield, 2019; Miralles et al., 2016). This advancement opens new opportunities for large scale studies of carbon- water relations on a diurnal time scale. The generation of the X-BASE ET_T product was facilitated by the development of site-level evapotranspiration partitioning methods (Nelson et al., 2018, 2020) underlining once more the importance of advances by the FLUXNET community for Earth system science.

5 Tackling persistent challenges

405 Next to these improvements and opportunities, we find that some key issues previously identified in FLUXCOM (Tramontana et al., 2016; Jung et al., 2020; Bodesheim et al., 2018) persist in X-BASE. These include the insufficient representation of water-related effects, the limited predictability of the spatial patterns of mean NEE , as well as severe limitations with respect to the variability between years and over decades. The overestimation of mean ET in very dry, sparsely vegetated areas (Fig. 410 B3), as well as the poorer consistency of NEE seasonality with inversions in water limited regions (Fig. 5) illustrate the persistent challenge and importance of capturing water effects on land-atmosphere flux variations. For GPP temporal patterns we find that X-BASE shows improved agreement with SIF in water limited regions compared to RS+METEO (Fig. 7), which is likely because X-BASE uses concomitantly changing remote sensing observations opposed to a mean seasonal cycle only in RS+METEO. However, X-BASE shows deteriorated agreement with SIF when compared to RS, even though X-BASE was 415 trained on hourly flux observations with improved coverage of dry conditions (Fig. 1). This decrease in performance indicates clearly the importance and uncertainty related to the predictor variable set for capturing water related effects. Thus, there is considerable potential for advancements by including remote sensing based predictors on soil moisture, sub-daily varying land surface temperature from geostationary satellites, SIF, and vegetation optical depth. Here, a key challenge resides in achieving a sensible integration of flux observations with footprints that are much smaller than corresponding Earth observation products.

420 Missing predictor variables is likely also a main reason for the limited skill of predicting between site variability of mean NEE (Fig. 2), which can depend on legacy effects of disturbances and management that are not accounted for. Novel and complementary Earth observation products that characterise ecosystem structure and states related to biomass and canopy heights from SAR and LIDAR should help raise the accuracy of FLUXCOM-X based mean NEE in future efforts. X-BASE shows a prominent pattern of carbon flux to the atmosphere in sub-tropical and crop dominated regions of India and the Sahel, 425 which emphasizes the need to improve in-situ data coverage for agricultural systems, especially outside the temperate zone, and including important meta-data to better characterize these ecosystems and their site history. Despite the greatly reduced overall bias of mean NEE , we emphasize that X-BASE products are pre-mature for diagnosing spatial variations of mean NEE .

430 The representation of longer term dynamics remains an area with opportunity for improvements in X-BASE. Inter-annual variability is still poorly reproduced in cross validation (Fig. 2), particularly for NEE , which is likely not only due to the complexity of processes shaping inter-annual variations but also due to temporal discontinuities in flux tower time series related to changes in instrumentation and factors like management (Jung et al., 2023) that are not accounted for. The complexities of



relying on field deployed instrumentation, together with the uncertainties related to linking satellite and flux data, causes poor signal to noise ratios and may impede good cross-validation results for i.a.v.. Globally, comparisons of X-BASE with inversions reveal an underestimated inter-annual variance and a poor correlation for global *NEE* i.a.v. (Fig. 5 and Table B2). Interestingly, 435 X-BASE *GPP* shows improved correspondence with SIF anomalies compared to RS+METEO, especially in water limited regions (Fig. 7), while no such improvement is evident for global *NEE*, which is likely due to the compensatory water effects in the global *NEE* signal (Jung et al., 2017). That a comparison of RS+METEO runs with different meteorological forcing data showed the weakest correspondence with inversion i.a.v. when using ERA5 (Jung et al., 2020) explains the substantially 440 better correlations of RS+METEO with inversions for *NEE* i.a.v. in earlier studies (Jung et al., 2017, 2020), and may also explain the poor correlation of X-BASE. Thus, testing if alternative meteorological forcing data can improve global *NEE* i.a.v. for X-BASE is an important next step. It remains unclear at this point if accurate inter-annual variations at site-level and globally can be achieved by the FLUXCOM approach in the near future. Additional constraints beyond FLUXNET such as atmospheric *CO₂* measurements (Upton et al., 2023) or theoretical considerations in the form of hybrid (Reichstein et al., 2019) or deep learning models (Camps-Valls et al., 2021) are promising and such endeavours should be fostered.

445 6 Conclusions

We presented X-BASE, a new set of global high-resolution data-driven products of land-atmosphere fluxes from the FLUXCOM approach. This represents a cornerstone of our developments of the FLUXCOM-X framework designed to explore and mitigate current limitations to up-scaling from site to global scale. Improvements of the eddy covariance data facilitated reconciling estimates of global terrestrial net carbon exchange from X-BASE with top-down atmospheric inversions, and allowed 450 for the first time the generation of a global data-driven estimate of ecosystem transpiration. Beyond fostering all activities to enhance quality and coverage of available flux tower observations, most promise for future advancements by FLUXCOM-X relates to the synergistic exploitation of complementary satellite data streams to better capture water-related, site-history, and management effects. This will be challenging as it requires developing strategies and methodologies to better integrate in-situ flux observations and spaceborne Earth observations with very heterogeneous acquisition properties and with spatial resolutions 455 that are often very coarse compared to flux tower footprints. The recent de-orbiting of the TERRA spacecraft requires employing alternative satellite missions where practical issues of data acquisition and conceptual issues related to temporal consistency and reduced overlap with FLUXNET records pose imminent challenges. With FLUXCOM-X we have prepared the ground for tackling these challenges which can facilitate up-to-date and accurate flux estimates and thereby contribute to increased understanding of the Earth system in the future.



460 **Appendix A: Details on processing of Earth Observation Data**

A1 Dynamic quality control and cutout size

The conditions in the pixels around a given EC station should best represent the conditions of the land surface in the area where the actual fluxes originate from. Given that the actual flux footprints are not generally available or computable for lack of critical information, we assume that the pixel containing the actual EC station (the ‘tower pixel’) is most representative 465 for the dynamics of the area of influence on a tower. However, data availability and quality in the tower pixel is often insufficient. An iterative approach therefore selects both the cutout size and the strictness of the BRDF inversion quality from within defined bounds in a way that maximizes data availability and that ensures representativeness of the spatially averaged time series for the given site at the same time. In more detail, we start with a strict criterion for BRDF inversion quality (BRDF_Albedo_Band_Quality_Bandx flag in MCD43A2 ≤ 2 , meaning only full inversions). Then three options regarding 470 the cutout size are considered:

- A) only the tower pixel,
- B) those 20% of pixels within $4 \times 4 \text{ km}^2$ around a tower that are best correlated with the tower pixel are linearly regressed against the tower pixel and subsequently spatially averaged,
- C) the 25% of pixels within a $4 \times 4 \text{ km}^2$ area that are closest to the tower are averaged with the inverse of the distance to the 475 tower as weight.

The criteria for selection between options A-C is based on the number of available good quality observations n in the resulting spatial average time series per site as follows:

```
if (n_A >= 60 %) & (n_B <= 70 %):  
    select A  
480 elif (n_A >= 60 %) & (n_B >= 70 %):  
    select B  
elif (n_A < 60 %) & (n_A > 15 %):  
    select B  
else:  
485    select C
```

If after the previous steps still less than 40% of good quality observations outside of snow covered times are available in the resulting average time series for a given site and index, the BRDF inversion quality threshold is relaxed to also allow magnitude inversions (MCD43A2 BRDF inversion quality flag ≤ 3), and the procedure to select the pixels contributing to the average described above is repeated. Consequently, the size of the area that a MODIS reflectance time series represents varies between 490 sites, and so does the BRDF inversion quality.



For the global gridded MODIS data, the BRDF inversion quality is consistently selected as <=2 or <=3 based on the number of available good quality observations in a pixel.

A2 Details on the treatment of land cover information

Land cover information was passed through an intermediary classification system to both act as an encoding mechanism and to 495 allow for arbitrary links between classification schemes. Rather than simple true/false classification for each category, different attributes are classified based on whether the classification has (value=1.0), might have (value=0.5), does not have (value=0.0) a specific feature, or is unknown (value=-1.0). In the specific case of the MCD12Q1 classification scheme, the conversion is as seen in Table A1.

Table A1: Land cover intermediary classification encoding for MCD12Q1 classifications.

	Trees	Shrubs	Grasses	Crops	Unveg	Water	Wetland	C4_photd	Managed	Needlele	Broadlea	Deciduo	Evergreen
ENF	1	0	0	0	0	0	0	0	-1	1	0	0	1
EBF	1	0	0	0	0	0	0	0	-1	0	1	0	1
DNF	1	0	0	0	0	0	0	0	-1	1	0	1	0
DBF	1	0	0	0	0	0	0	0	-1	0	1	1	0
MF	1	0	0	0	0	0	0	0	-1	-1	-1	-1	-1
CSH	0.5	1	0	0	0	0	0	-1	-1	-1	-1	-1	-1
OSH	0	1	0.5	0	0.5	0	0	-1	-1	-1	-1	-1	-1
WSA	1	0.5	0.5	0	0	0	0	-1	-1	-1	-1	-1	-1
SAV	0.5	0.5	1	0	0	0	0	-1	-1	-1	-1	-1	-1
GRA	0	0	1	0	0	0	0	-1	-1	0	0	0	0
SNO	-1	-1	-1	-1	0	0.5	1	0	0	-1	-1	-1	-1
CRO	0	0	0	1	0	0	0	-1	1	0	0	0	0
WET	0	0	0	0	0	1	0	0	0	0	0	0	0



Appendix B: Additional results

500 B1 Additional cross-validation results

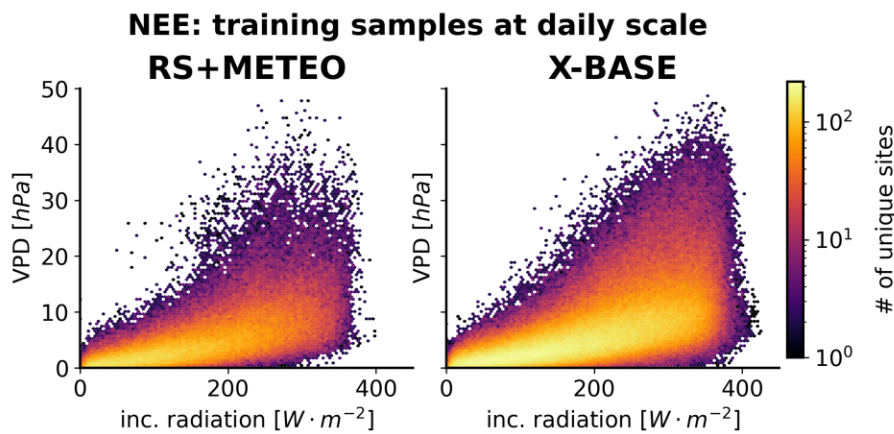


Figure B1. Cross-validation sampling in meteorological space: Number of unique sites contributing to sampling for *NEE* for FLUXCOM RS+METEO (left) compared to the sampling in the X-BASE set-up (right). Color corresponds to number of unique sites per bin in log scale.



B2 Large carbon uptake in tropical croplands

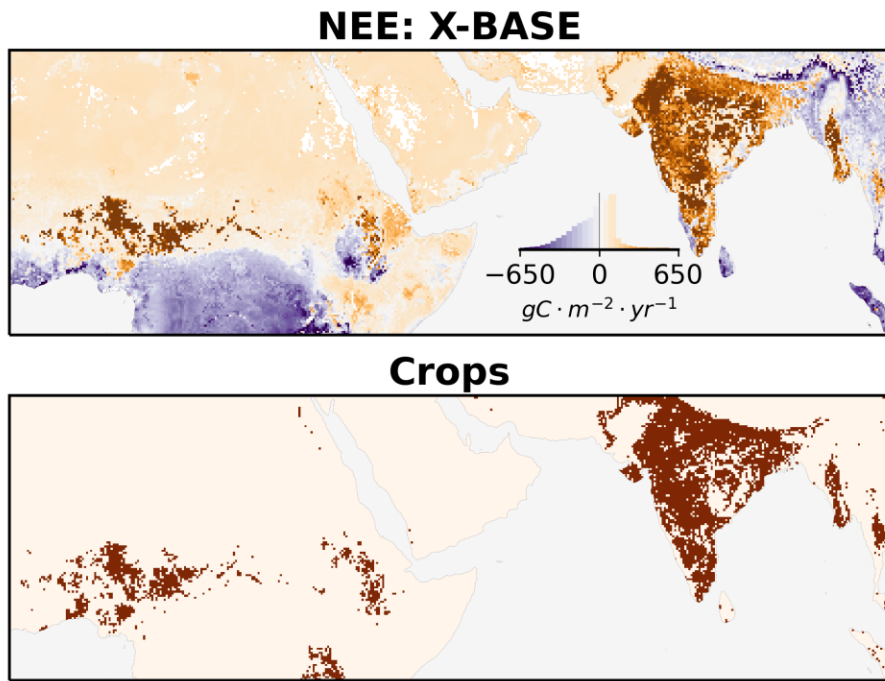


Figure B2. Large carbon uptake in tropical croplands



B3 Global magnitude of all fluxes

Table B1: **Global magnitude of all fluxes.** Column *Global Total* is the globally integrated flux for all areas including sparsely vegetated dry areas from 2001-2020. The column *Veg. Areas* includes a common mask which removes sparsely vegetated areas which are not computed for the RS and RS+METEO products. Values reported after the \pm correspond to the standard deviation across years.

	Global Total	Veg. Areas
NEE		
	$PgC \cdot yr^{-1}$	$PgC \cdot yr^{-1}$
X-BASE	-5.75 ± 0.33	-7.12 ± 0.32
RS+METEO	-	-21.27 ± 0.59
RS	-	-19.08 ± 0.93
CarboScope	-3.88 ± 0.84	-3.92 ± 0.84
GPP		
	$PgC \cdot yr^{-1}$	$PgC \cdot yr^{-1}$
X-BASE	124.7 ± 2.1	121.9 ± 2.0
RS+METEO	-	121.6 ± 0.4
RS	-	113.2 ± 1.8
ET		
	$km^3 \cdot yr^{-1}$	$km^3 \cdot yr^{-1}$
X-BASE	$74.7 \times 10^3 \pm 0.9 \times 10^3$	$68.9 \times 10^3 \pm 0.9 \times 10^3$
RS+METEO	-	$68.3 \times 10^3 \pm 0.3 \times 10^3$
RS	-	$78.5 \times 10^3 \pm 0.5 \times 10^3$
GLEAM	$72.5 \times 10^3 \pm 1.0 \times 10^3$	$70.9 \times 10^3 \pm 0.9 \times 10^3$
ET_T		
	$km^3 \cdot yr^{-1}$	$km^3 \cdot yr^{-1}$
X-BASE	$42.6 \times 10^3 \pm 1.0 \times 10^3$	$41.8 \times 10^3 \pm 0.9 \times 10^3$
GLEAM	$50.7 \times 10^3 \pm 0.6 \times 10^3$	$50.7 \times 10^3 \pm 0.6 \times 10^3$
ET_T/ET		
X-BASE	$57.0\% \pm 0.6\%$	$60.7\% \pm 0.6\%$
GLEAM	$70.0\% \pm 0.6\%$	$71.4\% \pm 0.6\%$



B4 Linear trends and inter-annual variability for all fluxes

Table B2: **Long-term variability of fluxes.** Column *linear trend* is the linear slope of annually integrated fluxes over the years 2001-2020. The column *inter-annual variability* is computed as the standard deviation of annually integrated fluxes after the trend is removed.

	Linear Trend	Inter-annual Variability
NEE		
	$PgC \cdot yr^{-2}$	$PgC \cdot yr^{-1}$
X-BASE	0.017	0.306
RS+METEO	0.095	0.229
RS	-0.129	0.557
CarboScope	0.006	0.837
GPP		
	$PgC \cdot yr^{-2}$	$PgC \cdot yr^{-1}$
X-BASE	0.340	0.575
RS+METEO	-0.053	0.246
RS	0.248	1.023
ET		
	$km^3 \cdot yr^{-2}$	$km^3 \cdot yr^{-1}$
X-BASE	0.144x10 ³	0.331x10 ³
RS+METEO	-0.010x10 ³	0.301x10 ³
RS	0.053x10 ³	0.392x10 ³
GLEAM	0.102x10 ³	0.730x10 ³
ET_T		
	$km^3 \cdot yr^{-2}$	$km^3 \cdot yr^{-1}$
X-BASE	0.158x10 ³	0.277x10 ³
GLEAM	0.035x10 ³	0.596x10 ³
ET_T/ET		
	$\% \cdot yr^{-1}$	$\%$
X-BASE	0.102%	0.157%
GLEAM	-0.054%	0.452%



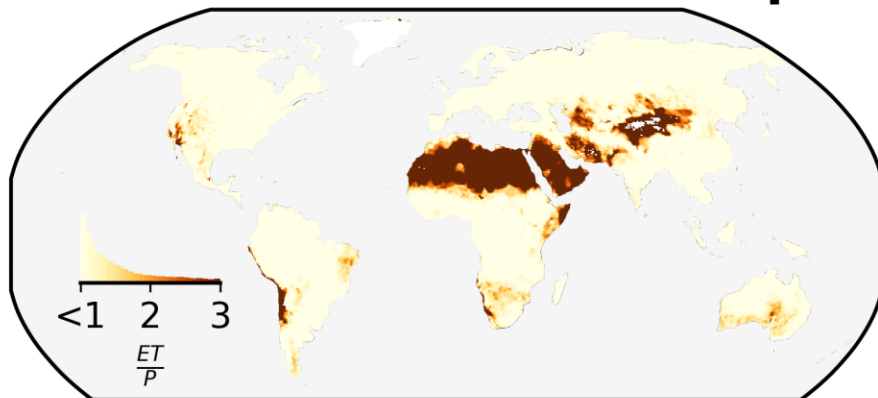
B5 Potential overestimation of ET in dryland areas

505 Maps in Fig. B3 show the extend where ET and ET_T exceed precipitation as the ratio between the total of each flux to total precipitation (from GPCC Schneider et al. (2022)). Overall, X-BASE ET largely exceeds precipitation in most dry, sparsely vegetated areas, indicating overestimation. In contrast, ET_T does not show such extensive overestimation, limited instead to only smaller regions of the Sahara.

510 The amount of overestimation of X-BASE ET can be roughly estimated by replacing areas where annual ET exceeds precipitation inputs with the corresponding annual precipitation inputs for each grid cell, i.e. replacing areas where the $ET/precip$ ratio is more than a threshold with the precipitation rather than the estimated ET . Using thresholds from 1.25 to 2.5 gives an excess of ET (i.e. original ET minus precipitation corrected) from 3.9×10^3 to $6.1 \times 10^3 \text{ km}^3 \cdot \text{yr}^{-1}$.



X-BASE ET ratio to Precip.



X-BASE ET_T ratio to Precip.

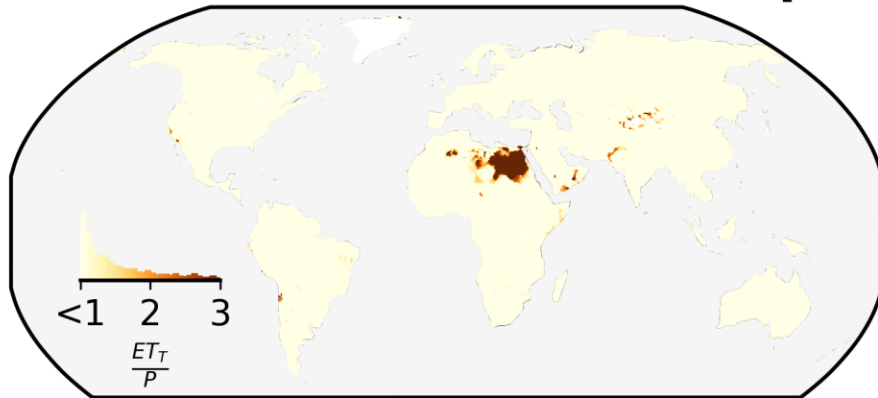


Figure B3. Potential ET overestimation based on the ratio of estimated ET to precipitation from the Global Precipitation Climatology Centre (GPCC Schneider et al. (2022)).



515 *Data availability.* All data is available as aggregated NetCDF file formats, to ease data handling for common use cases, from the ICOS Carbon Portal (<https://doi.org/10.18160/5NZG-JMJE>). Furthermore, the full resolution data is accessible in the zarr format and in a publicly available object store provided by German Climate Computing Center (Deutsches Klimarechenzentrum, DKRZ). Instructions on how to all data, as well as the full dataset, can be found at the associated repository (<https://gitlab.gwdg.de/fluxcom/fluxcomxdata>).

520 *Author contributions.* JN, SW and MJ wrote the manuscript, and all authors contributed to the editing and structuring of it. JN, SW, FG, BK, ZH wrote the code which constitutes the modeling environment FLUXCOM-X, structuring it according to discussions including MJ, UW, GD, and MM. Editorial input was provided by AI, AK, AS, BB, BK, DB, DP, FT, GCV, GD, GN, GW, JA, JC, KI, KMK, KN, LH, LS, MK, MM, MR, NB, RLS, SS, TT, and WZ. All other authors contributed through their work at one or more eddy-covariance stations through the acquisition of funding, set-up and maintenance, pre-processing and quality control, administration, and their insertion into regional or global networks.

Competing interests. We declare that one or more of the coauthors of this manuscript is a member of the editorial board of Biogeosciences.

525 *Acknowledgements.* We would like to thank the broader eddy covariance community, including FLUXNET and the associated regional networks, particularly the European Integrated Carbon Observation System (ICOS) and AmeriFlux. We also acknowledge the contributions of Andrej Varlagin and colleagues to these efforts. We thank the team at the ICOS Carbon Portal for their support in publishing the FLUXCOM-X data sets, with great thanks in particular to Ute Karstens and Zois Zogopoulos. We also thank Brendan Byrne and colleagues of Jet Propulsion Laboratory, California Institute of Technology, Pasadena, CA, USA for use of the OCO2 data. The work of S. Walther, J. A. Nelson and M. Jung was funded in part by European Union's Horizon 2020 research and innovation program (grant no. 776186 CHE, 530 776810 VERIFY, 958927 CoCO2, 820852 E-SHAPE). S. Walther acknowledges funding from an European Space Agency Living Planet Fellowship in the project Vad3e mecum as well as the CCI LST project (4000123553/18/I-NB). G. Duveiller and Z. M. Hamdi acknowledge funding from the European Space Agency in the Sen4GPP project (4000134598/21/I-NB). G. Duveiller acknowledges Horizon Europe funding (Open Earth Monitor Cyberinfrastructure project, 101059548). D. Zona acknowledges NSF award numbers 2149988 and 1932900. A. Klosterhalfen and A. Knohl acknowledge funding by the German Federal Ministry of Education and Research (BMBF) as part of the 535 European Integrated Carbon Observation System (ICOS), by the Deutsche Forschungsgemeinschaft (INST 186/1118-1 FUGG) and by the Ministry of Lower-Saxony for Science and Culture (DigitalForst: Niedersächsisches Vorab (ZN 3679)). L. Montagnani acknowledges funding provided by Forest Services, Autonomous Province of Bolzano. E. Yepez acknowledges that MX-Tes is part of the MexFlux regional network. Funding for the Swiss sites is greatly acknowledged from various sources: from the EU project SUPER-G (contract no. 774124), the SNF projects M4P (40FA40_154245), DiRad (146373), InnoFarm (407340_172433), CoCo (200021_197357), ICOS-CH (20FI21_148992, 540 20FI20_173691, 20FI20_198227) and InsuranceGrass (100018L_200918), from NESTLE via the ETH foundation (DONA), from the ETH Board and from ETH Zurich (project FEVER ETH-27 19-1). Funding for US-BZB, US-BZF, US-BZo, and US-BZB was provided by National Science Foundation Grants DEB LTREB 1354370 and 2011257, DEB-0425328, DEB-0724514, and DEB-0830997, as well as funding by the US Geological Survey Climate R&D program. Bonanza Creek Long Term Experimental Research station provided lab space, equip-



ment. US-ICs and US-ICt were supported by the grants from the Arctic Observatory Program of the National Science Foundation (grant numbers 1936752, 1503912, 1107892). S. Aranda-Barranco acknowledges the projects PID2020-117825GB-C21 and PID2020-117825GB-C22 funded by MCIN/AEI/10.13039/501100011033, as well as support by the FPU grant by the Ministry of Universities of Spain (REF: FPU19/01647). SE-Deg, SE-Svb and SE-Ros acknowledge funding from the Swedish Research Council, and contributing research institutes to the Swedish Integrated Carbon Observation System (ICOS-Sweden) Research Infrastructure and the Swedish Infrastructure for Ecosystem Science (SITES). T. Tagesson was funded by the Swedish National Space Agency (SNSA Dnr 2021-00144), and FORMAS (Dnr. 2021-00644). W. Woodgate is supported by an Australian Research Council DECRA Fellowship (DE190101182). I. Mammarella acknowledges funding from Academy of Finland (N-PERM 341349), ICOS-Finland UH, EU projects (GreenFeedback 101056921, LiweFor). D. Vitale acknowledges the Integrated Carbon Observation System - Research Infrastructure (ICOS ERIC, <https://www.icos-cp.eu/>) and the ICOS ETC funding from the Italian Ministry of Research. M. Göckede was supported by the European Research Council (ERC) under the European Union's Horizon 2020 research and innovation programme (grant agreement No 951288, Q-Arctic). S. Sabbatini acknowledges OEMC project - Grant agreement ID: 101059548. The DE-Geb site received funds within the ICOS Germany preparatory and implementation phase by the Federal Ministry of Education and Research and is supported by the Ministry of Digital and Traffic through ICOS station contributions as well as by the Ministry of Food and Agriculture covering operational costs. G. Gerosa thanks the Catholic University of Brescia for continuous supporting the research station of Bosco Fontana (ICOS station IT-Bft). L. Šigut acknowledges support by the Ministry of Education, Youth and Sports of CR within the CzeCOS program (grant number LM2023048). G. Camps-Valls would like 555 to acknowledge the support from the European Research Council (ERC) under the ERC Synergy Grant USMILE (grant agreement 855187). A. Desai acknowledges the US Dept of Energy American Network Management Project award to ChEAS core site cluster (US-PFa, US-WCr, US-Syv, US-Los), Wisconsin Potato and Vegetable Growers Association and WI Dept of Natural Resources (US-CS*), NSF 1822420, 560 2313772 (US-PFa). M. Roland and B. Gielen acknowledge the Research Foundation Flanders (FWO) for the support of ICOS research infrastructure in Flanders, Belgium. D. Papale thanks the support of the ITINERIS - Italian Integrated Environmental Research Infrastructures 565 System project (IR0000032) funded by Next Generation EU Mission 4.2.3.1. T. Vesala acknowledges ICOS-Finland (University of Helsinki) and Flagship funding (grant no. 337549). T. Sachs acknowledges that the DE-Zrk site relies on infrastructure of the Terrestrial Environmental Observatories Network (TERENO) supported by a Helmholtz Young Investigators Grant (VH-NG-821). E. Pendall acknowledges Australian 570 Terrestrial Ecosystem Research Network, as part of the National Cooperative Research Infrastructure System. S. Knox was also support by an NSERC Discovery Grant (RGPIN-2019-04199) and Alliance Grant (ALLRP 555468-20). H. Kobayashi acknowledges ArCSII No. JP-MXD1420318865 (US-Prr). S. Metzger acknowledges the National Ecological Observatory Network, which is a program sponsored by the National Science Foundation and operated under cooperative agreement by Battelle. This material is based in part upon work supported by the National Science Foundation through the NEON Program. B. Heinesch and C. Vincke acknowledge the Service Public de Wallonie (SPW-DGO6) for the support of ICOS research infrastructure in Wallonia, Belgium.



References

575 Amiro, B.: FLUXNET2015 CA-SF2 Saskatchewan - Western Boreal, Forest Burned in 1989, 2016a.
Amiro, B.: FLUXNET2015 CA-Man Manitoba - Northern Old Black Spruce (Former BOREAS Northern Study Area), 2016b.
Amiro, B.: FLUXNET2015 CA-SF1 Saskatchewan - Western Boreal, Forest Burned in 1977, 2016c.
Amiro, B.: FLUXNET2015 CA-SF3 Saskatchewan - Western Boreal, Forest Burned in 1998, 2016d.
Ammann, C.: FLUXNET2015 CH-Oe1 Oensingen Grassland, 2016.

580 Arain, M.: AmeriFlux FLUXNET-1F CA-TPD Ontario - Turkey Point Mature Deciduous, 2022a.
Arain, M.: AmeriFlux FLUXNET-1F CA-TP3 Ontario - Turkey Point 1974 Plantation White Pine, 2022b.
Arain, M. A.: FLUXNET2015 CA-TP2 Ontario - Turkey Point 1989 Plantation White Pine, 2016a.
Arain, M. A.: FLUXNET2015 CA-TP1 Ontario - Turkey Point 2002 Plantation White Pine, 2016b.
Arain, M. A.: FLUXNET2015 CA-TP4 Ontario - Turkey Point 1939 Plantation White Pine, 2016c.

585 Ardö, J., El Tahir, B. A., and ElKhidir, H. A. M.: FLUXNET2015 SD-Dem Demokeya, 2016.
Arndt, S., Hinko-Najera, N., and Griebel, A.: FLUXNET2015 AU-Wom Wombat, 2016.
Aurela, M., Lohila, A., Tuovinen, J.-P., Hatakka, J., Rainne, J., Mäkelä, T., and Lauria, T.: FLUXNET2015 FI-Lom Lompolojankka, 2016a.
Aurela, M., Tuovinen, J.-P., Hatakka, J., Lohila, A., Mäkelä, T., Rainne, J., and Lauria, T.: FLUXNET2015 FI-Sod Sodankyla, 2016b.
Badgley, G., Field, C. B., and Berry, J. A.: Canopy Near-Infrared Reflectance and Terrestrial Photosynthesis, *Science Advances*, 3, 2017.

590 Baker, J. and Griffis, T.: AmeriFlux FLUXNET-1F US-Ro5 Rosemount I18_South, 2021.
Baker, J. and Griffis, T.: AmeriFlux FLUXNET-1F US-Ro4 Rosemount Prairie, 2022a.
Baker, J. and Griffis, T.: AmeriFlux FLUXNET-1F US-Ro6 Rosemount I18_North, 2022b.
Baker, J., Griffis, T., and Griffis, T.: AmeriFlux FLUXNET-1F US-Ro1 Rosemount- G21, 2022.
Balocchi, D.: FLUXNET2015 US-Twt Twitchell Island, 2016.

595 Balocchi, D. and Ma, S.: FLUXNET2015 US-Ton Tonzi Ranch, 2016.
Balocchi, D. and Penuelas, J.: The Physics and Ecology of Mining Carbon Dioxide from the Atmosphere by Ecosystems, *Global Change Biology*, 25, 1191–1197, 2019.
Balocchi, D., Ma, S., and Xu, L.: FLUXNET2015 US-Var Vaira Ranch- Ione, 2016.
Balocchi, D. D.: How Eddy Covariance Flux Measurements Have Contributed to Our Understanding of *Global Change Biology*, *Global*

600 *Change Biology*, 26, 242–260, 2019.
Bao, S., Wutzler, T., Koirala, S., Cuntz, M., Ibrom, A., Besnard, S., Walther, S., Šigut, L., Moreno, A., Weber, U., Wohlfahrt, G., Cleverly, J., Migliavacca, M., Woodgate, W., Merbold, L., Veenendaal, E., and Carvalhais, N.: Environment-Sensitivity Functions for Gross Primary Productivity in Light Use Efficiency Models, *Agricultural and Forest Meteorology*, 312, 108 708, 2022.
Belelli, L., Papale, D., and Valentini, R.: FLUXNET2015 RU-Ha1 Hakasia Steppe, 2016.

605 Berbigier, P. and Loustau, D.: FLUXNET2015 FR-LBr Le Bray, 2016.
Berg, A. and Sheffield, J.: Evapotranspiration Partitioning in CMIP5 Models: Uncertainties and Future Projections, *Journal of Climate*, 32, 2653–2671, 2019.
Beringer, J. and Hutley, L.: FLUXNET2015 AU-Fog Fogg Dam, 2016a.
Beringer, J. and Hutley, L.: FLUXNET2015 AU-DaP Daly River Savanna, 2016b.

610 Beringer, J. and Hutley, L.: FLUXNET2015 AU-Ade Adelaide River, 2016c.



Beringer, J. and Hutley, L.: FLUXNET2015 AU-RDF Red Dirt Melon Farm, Northern Territory, 2016d.

Beringer, J. and Hutley, L.: FLUXNET2015 AU-Dry Dry River, 2016e.

Beringer, J. and Hutley, P. L.: FLUXNET2015 AU-DaS Daly River Cleared, 2016f.

Beringer, J. and Walker, J.: FLUXNET2015 AU-Ync Jaxa, 2016.

615 Beringer, J., Cunningham, S., Baker, P., Cavagnaro, T., MacNally, R., Thompson, R., and McHugh, I.: FLUXNET2015 AU-Whr Whroo, 2016a.

Beringer, J., Hutley, L., McGuire, D., and U, P.: FLUXNET2015 AU-Wac Wallaby Creek, 2016b.

Bernhofer, C., Grünwald, T., Moderow, U., Hehn, M., Eichelmann, U., and Prasse, H.: FLUXNET2015 DE-Spw Spreewald, 2016.

Billesbach, D., Bradford, J., and Torn, M.: FLUXNET2015 US-AR2 ARM USDA UNL OSU Woodward Switchgrass 2, 2016a.

620 Billesbach, D., Bradford, J., and Torn, M.: FLUXNET2015 US-AR1 ARM USDA UNL OSU Woodward Switchgrass 1, 2016b.

Billesbach, D., Kueppers, L., Torn, M., and Biraud, S.: AmeriFlux FLUXNET-1F US-A32 ARM-SGP Medford Hay Pasture, 2022.

Biraud, S., Fischer, M., Chan, S., and Torn, M.: AmeriFlux FLUXNET-1F US-ARM ARM Southern Great Plains Site- Lamont, 2022.

Black, T.: AmeriFlux FLUXNET-1F CA-LP1 British Columbia - Mountain Pine Beetle-Attacked Lodgepole Pine Stand, 2021.

Black, T. A.: FLUXNET2015 CA-Obs Saskatchewan - Western Boreal, Mature Black Spruce, 2016a.

625 Black, T. A.: FLUXNET2015 CA-Oas Saskatchewan - Western Boreal, Mature Aspen, 2016b.

Blanken, P., Monson, R., Burns, S., Bowling, D., and Turnipseed, A.: AmeriFlux FLUXNET-1F US-NR1 Niwot Ridge Forest (LTER NWT1), 2022.

Bodesheim, P., Jung, M., Gans, F., Mahecha, M. D., and Reichstein, M.: Upscaled Diurnal Cycles of Land–Atmosphere Fluxes: A New Global Half-Hourly Data Product, *Earth System Science Data*, 10, 1327–1365, 2018.

630 Bohrer, G.: AmeriFlux FLUXNET-1F US-ORv Olentangy River Wetland Research Park, 2021.

Bohrer, G.: AmeriFlux FLUXNET-1F US-UM3 Douglas Lake, 2022.

Bohrer, G. and Kerns, J.: AmeriFlux FLUXNET-1F US-OWC Old Woman Creek, 2022.

Boike, J., Westermann, S., Lüers, J., Langer, M., and Piel, K.: FLUXNET2015 SJ-Blv Bayelva, Spitsbergen, 2016.

Bonan, G. B., Lawrence, P. J., Oleson, K. W., Levis, S., Jung, M., Reichstein, M., Lawrence, D. M., and Swenson, S. C.: Improving Canopy 635 Processes in the Community Land Model Version 4 (CLM4) Using Global Flux Fields Empirically Inferred from FLUXNET Data, *Journal of Geophysical Research*, 116, 2011.

Bowling, D.: FLUXNET2015 US-Cop Corral Pocket, 2016.

Brunsell, N.: AmeriFlux FLUXNET-1F US-KFS Kansas Field Station, 2022a.

Brunsell, N.: AmeriFlux FLUXNET-1F US-KLS Kansas Land Institute, 2022b.

640 Burton, C. A., Renzullo, L. J., Rifai, S. W., and Van Dijk, A. I. J. M.: Empirical Upscaling of OzFlux Eddy Covariance for High-Resolution Monitoring of Terrestrial Carbon Uptake in Australia, 2023.

Byrne, B., Baker, D. F., Basu, S., Bertolacci, M., Bowman, K. W., Carroll, D., Chatterjee, A., Chevallier, F., Ciais, P., Cressie, N., Crisp, D., Crowell, S., Deng, F., Deng, Z., Deutscher, N. M., Dubey, M. K., Feng, S., García, O. E., Griffith, D. W. T., Herkommmer, B., Hu, L., Jacobson, A. R., Janardanan, R., Jeong, S., Johnson, M. S., Jones, D. B. A., Kivi, R., Liu, J., Liu, Z., Maksyutov, S., Miller, J. B., Miller, 645 S. M., Morino, I., Notholt, J., Oda, T., O'Dell, C. W., Oh, Y.-S., Ohyama, H., Patra, P. K., Peiro, H., Petri, C., Philip, S., Pollard, D. F., Poulter, B., Remaud, M., Schuh, A., Sha, M. K., Shiomi, K., Strong, K., Sweeney, C., Té, Y., Tian, H., Velazco, V. A., Vrekoussis, M., Warneke, T., Worden, J. R., Wunch, D., Yao, Y., Yun, J., Zammit-Mangion, A., and Zeng, N.: National CO₂ Budgets (2015–2020) Inferred from Atmospheric CO₂ Observations in Support of the Global Stocktake, *Earth System Science Data*, 15, 963–1004, 2023.



650 Camps-Valls, G., Tuia, D., Zhu, X. X., and Reichstein, M.: Deep Learning for the Earth Sciences: A Comprehensive Approach to Remote Sensing, Climate Science, and Geosciences, Wiley, 1 edn., 2021.

Cescatti, A., Marcolla, B., Zorer, R., and Gianelle, D.: FLUXNET2015 IT-La2 Lavarone2, 2016.

Chamberlain, S., Oikawa, P., Sturtevant, C., Szutu, D., Verfaillie, J., and Baldocchi, D.: AmeriFlux FLUXNET-1F US-Tw3 Twitchell Alfalfa, 2022.

Chen, J.: FLUXNET2015 US-Wi5 Mixed Young Jack Pine (MYJP), 2016a.

655 Chen, J.: FLUXNET2015 US-Wi3 Mature Hardwood (MHW), 2016b.

Chen, J.: FLUXNET2015 US-Wi8 Young Hardwood Clearcut (YHW), 2016c.

Chen, J.: FLUXNET2015 US-Wi4 Mature Red Pine (MRP), 2016d.

Chen, J.: FLUXNET2015 US-Wi1 Intermediate Hardwood (IHW), 2016e.

Chen, J.: FLUXNET2015 US-Wi9 Young Jack Pine (YJP), 2016f.

660 Chen, J.: FLUXNET2015 US-Wi0 Young Red Pine (YRP), 2016g.

Chen, J.: FLUXNET2015 US-Wi6 Pine Barrens #1 (PB1), 2016h.

Chen, J.: FLUXNET2015 US-Wi7 Red Pine Clearcut (RPCC), 2016i.

Chen, J.: FLUXNET2015 US-Wi2 Intermediate Red Pine (IRP), 2016j.

Chen, J. and Chu, H.: FLUXNET2015 US-WPT Winous Point North Marsh, 2016a.

665 Chen, J. and Chu, H.: FLUXNET2015 US-CRT Curtice Walter-Berger Cropland, 2016b.

Chen, J., Chu, H., and Noormets, A.: FLUXNET2015 US-Oho Oak Openings, 2016.

Chen, S.: FLUXNET2015 CN-Du2 Duolun_grassland (D01), 2016k.

Chen, T. and Guestrin, C.: XGBoost, in: Proceedings of the 22nd ACM SIGKDD International Conference on Knowledge Discovery and Data Mining, ACM, 2016.

670 Christen, A. and Knox, S.: AmeriFlux FLUXNET-1F CA-DBB Delta Burns Bog, 2022.

Christensen, T.: FLUXNET2015 SJ-Adv Adventdalen, 2016.

Cleverly, J. and Eamus, D.: FLUXNET2015 AU-TTE Ti Tree East, 2016a.

Cleverly, J. and Eamus, D.: FLUXNET2015 AU-ASM Alice Springs, 2016b.

Coenders-Gerrits, A. M. J., van der Ent, R. J., Bogaard, T. A., Wang-Erlandsson, L., Hrachowitz, M., and Savenije, H. H. G.: Uncertainties 675 in Transpiration Estimates, *Nature*, 506, E1–E2, 2014.

Dannenberg, M. P., Barnes, M. L., Smith, W. K., Johnston, M. R., Meerdink, S. K., Wang, X., Scott, R. L., and Biederman, J. A.: Upscaling Dryland Carbon and Water Fluxes with Artificial Neural Networks of Optical, Thermal, and Microwave Satellite Remote Sensing, *Biogeosciences*, 20, 383–404, 2023.

Desai, A.: FLUXNET2015 US-WCr Willow Creek, 2016a.

680 Desai, A.: FLUXNET2015 US-Syv Sylvania Wilderness Area, 2016b.

Desai, A.: FLUXNET2015 US-Los Lost Creek, 2016c.

Desai, A.: FLUXNET2015 US-PFa Park Falls/WLEF, 2016d.

Desai, A.: AmeriFlux FLUXNET-1F US-CS1 Central Sands Irrigated Agricultural Field, 2022a.

Desai, A.: AmeriFlux FLUXNET-1F US-CS4 Central Sands Irrigated Agricultural Field, 2022b.

685 Desai, A.: AmeriFlux FLUXNET-1F US-CS2 Tri County School Pine Forest, 2022c.

Desai, A.: AmeriFlux FLUXNET-1F US-CS3 Central Sands Irrigated Agricultural Field, 2022d.



Dolman, H., Hendriks, D., Parmentier, F.-J., Marchesini, L. B., Dean, J., and Van Huissteden, K.: FLUXNET2015 NL-Hor Horstermeer, 2016a.

Dolman, H., Van Der Molen, M., Parmentier, F.-J., Marchesini, L. B., Dean, J., Van Huissteden, K., and Maximov, T.: FLUXNET2015 690 RU-Cok Chokurdakh, 2016b.

Dong, G.: FLUXNET2015 CN-Cng Changling, 2016.

Drake, B. and Hinkle, R.: FLUXNET2015 US-KS1 Kennedy Space Center (Slash Pine), 2016a.

Drake, B. and Hinkle, R.: FLUXNET2015 US-KS2 Kennedy Space Center (Scrub Oak), 2016b.

Euskirchen, E.: AmeriFlux FLUXNET-1F US-BZo Bonanza Creek Old Thermokarst Bog, 2022a.

695 Euskirchen, E.: AmeriFlux FLUXNET-1F US-BZB Bonanza Creek Thermokarst Bog, 2022b.

Euskirchen, E.: AmeriFlux FLUXNET-1F US-BZF Bonanza Creek Rich Fen, 2022c.

Euskirchen, E.: AmeriFlux FLUXNET-1F US-BZS Bonanza Creek Black Spruce, 2022d.

Euskirchen, E., Shaver, G., and Bret-Harte, S.: AmeriFlux FLUXNET-1F US-ICs Imnavait Creek Watershed Wet Sedge Tundra, 2022a.

Euskirchen, E., Shaver, G., and Bret-Harte, S.: AmeriFlux FLUXNET-1F US-ICt Imnavait Creek Watershed Tussock Tundra, 2022b.

700 Ewers, B. and Pendall, E.: FLUXNET2015 US-Sta Saratoga, 2016.

Fares, S.: FLUXNET2015 US-Lin Lindeove Orange Orchard, 2016.

Flerchinger, G.: AmeriFlux FLUXNET-1F US-Rwf RCEW Upper Sheep Prescribed Fire, 2022a.

Flerchinger, G.: AmeriFlux FLUXNET-1F US-Rws Reynolds Creek Wyoming Big Sagebrush, 2022b.

Flerchinger, G.: AmeriFlux FLUXNET-1F US-Rms RCEW Mountain Big Sagebrush, 2022c.

705 Flerchinger, G. and Reba, M.: AmeriFlux FLUXNET-1F US-Rwe RCEW Reynolds Mountain East, 2022.

Forsythe, J., Kline, M., and O'Halloran, T.: AmeriFlux FLUXNET-1F US-HB1 North Inlet Crab Haul Creek, 2021.

Friedl, M. and Sulla-Menashe, D.: MCD12Q1 MODIS/Terra+Aqua Land Cover Type Yearly L3 Global 500m SIN Grid V006, 2019.

Fu, Z., Gerken, T., Bromley, G., Araújo, A., Bonal, D., Burban, B., Ficklin, D., Fuentes, J. D., Goulden, M., Hirano, T., Kosugi, Y., Liddell, 710 M., Nicolini, G., Niu, S., Rouspard, O., Stefani, P., Mi, C., Tofte, Z., Xiao, J., Valentini, R., Wolf, S., and Stoy, P. C.: The Surface-Atmosphere Exchange of Carbon Dioxide in Tropical Rainforests: Sensitivity to Environmental Drivers and Flux Measurement Methodology, *Agricultural and Forest Meteorology*, 263, 292–307, 2018.

Gao, B.-c.: NDWI—A Normalized Difference Water Index for Remote Sensing of Vegetation Liquid Water from Space, *Remote Sensing of Environment*, 58, 257–266, 1996.

Garcia, A., Di Bella, C., Houspanossian, J., Magliano, P., Jobbág, E., Posse, G., Fernández, R., and Noso, M.: FLUXNET2015 AR-SLu 715 San Luis, 2016.

Gash, J. H. C.: An Analytical Model of Rainfall Interception by Forests, *Quarterly Journal of the Royal Meteorological Society*, 105, 43–55, 1979.

Goldstein, A.: FLUXNET2015 US-Blo Blodgett Forest, 2016.

Good, S. P., Noone, D., and Bowen, G.: Hydrologic Connectivity Constrains Partitioning of Global Terrestrial Water Fluxes, *Science*, 349, 720 175–177, 2015.

Goslee, S.: AmeriFlux FLUXNET-1F US-HWB USDA ARS Pasture Systems and Watershed Management Research Unit- Hawbecker Site, 2022.

Gough, C., Bohrer, G., and Curtis, P.: FLUXNET2015 US-UMB Univ. Of Mich. Biological Station, 2016.

Gough, C., Bohrer, G., and Curtis, P.: AmeriFlux FLUXNET-1F US-UMd UMBS Disturbance, 2022.



725 Goulden, M.: FLUXNET2015 CA-NS2 UCI-1930 Burn Site, 2016a.
Goulden, M.: FLUXNET2015 CA-NS3 UCI-1964 Burn Site, 2016b.
Goulden, M.: FLUXNET2015 CA-NS4 UCI-1964 Burn Site Wet, 2016c.
Goulden, M.: FLUXNET2015 BR-Sa3 Santarem-Km83-Logged Forest, 2016d.
Goulden, M.: FLUXNET2015 CA-NS6 UCI-1989 Burn Site, 2016e.

730 Goulden, M.: FLUXNET2015 CA-NS7 UCI-1998 Burn Site, 2016f.
Goulden, M.: FLUXNET2015 CA-NS5 UCI-1981 Burn Site, 2016g.
Griffis, T. and Roman, T.: AmeriFlux FLUXNET-1F PE-QFR Quistococha Forest Reserve, 2021.
Gruening, C., Goded, I., Cescatti, A., Manca, G., and Seufert, G.: FLUXNET2015 IT-SRo San Rossore, 2016a.
Gruening, C., Goded, I., Cescatti, A., and Pokorska, O.: FLUXNET2015 IT-Isp Ispra ABC-IS, 2016b.

735 Hansen, B. U.: FLUXNET2015 GL-NuF Nuuk Fen, 2016.
Heinsch, F., Zhao, M., Running, S., Kimball, J., Nemani, R., Davis, K., Bolstad, P., Cook, B., Desai, A., Ricciuto, D., Law, B., Oechel, W., Kwon, H., Luo, H., Wofsy, S., Dunn, A., Munger, J., Baldocchi, D., Xu, L., Hollinger, D., Richardson, A., Stoy, P., Siqueira, M., Monson, R., Burns, S., and Flanagan, L.: Evaluation of Remote Sensing Based Terrestrial Productivity from MODIS Using Regional Tower Eddy Flux Network Observations, *IEEE Transactions on Geoscience and Remote Sensing*, 44, 1908–1925, 2006.

740 Hersbach, H., Bell, B., Berrisford, P., Hirahara, S., Horányi, A., Muñoz-Sabater, J., Nicolas, J., Peubey, C., Radu, R., Schepers, D., Simmons, A., Soci, C., Abdalla, S., Abellán, X., Balsamo, G., Bechtold, P., Biavati, G., Bidlot, J., Bonavita, M., Chiara, G., Dahlgren, P., Dee, D., Diamantakis, M., Dragani, R., Flemming, J., Forbes, R., Fuentes, M., Geer, A., Haimberger, L., Healy, S., Hogan, R. J., Hólm, E., Janisková, M., Keeley, S., Laloyaux, P., Lopez, P., Lupu, C., Radnoti, G., Rosnay, P., Rozum, I., Vamborg, F., Villaume, S., and Thépaut, J.: The ERA5 Global Reanalysis, *Quarterly Journal of the Royal Meteorological Society*, 146, 1999–2049, 2020.

745 Hinkle, R.: AmeriFlux FLUXNET-1F US-KS3 Kennedy Space Center (Salt Marsh), 2022.
Hollinger, D.: AmeriFlux FLUXNET-1F US-Ho2 Howland Forest (West Tower), 2022.

Huang, X., Xiao, J., Wang, X., and Ma, M.: Improving the Global MODIS GPP Model by Optimizing Parameters with FLUXNET Data, *Agricultural and Forest Meteorology*, 300, 108 314, 2021.

750 Huete, A., Didan, K., Miura, T., Rodriguez, E., Gao, X., and Ferreira, L.: Overview of the Radiometric and Biophysical Performance of the MODIS Vegetation Indices, *Remote Sensing of Environment*, 83, 195–213, 2002.

Huggins, D.: AmeriFlux FLUXNET-1F US-CF1 CAF-LTAR Cook East, 2021.
Huggins, D.: AmeriFlux FLUXNET-1F US-CF3 CAF-LTAR Boyd North, 2022a.
Huggins, D.: AmeriFlux FLUXNET-1F US-CF4 CAF-LTAR Boyd South, 2022b.
Huggins, D.: AmeriFlux FLUXNET-1F US-CF2 CAF-LTAR Cook West, 2022c.

755 Ichii, K., Ueyama, M., Kondo, M., Saigusa, N., Kim, J., Alberto, M. C., Ardö, J., Euskirchen, E. S., Kang, M., Hirano, T., Joiner, J., Kobayashi, H., Marchesini, L. B., Merbold, L., Miyata, A., Saitoh, T. M., Takagi, K., Varlagin, A., Bret-Harte, M. S., Kitamura, K., Kosugi, Y., Kotani, A., Kumar, K., Li, S., Machimura, T., Matsuura, Y., Mizoguchi, Y., Ohta, T., Mukherjee, S., Yanagi, Y., Yasuda, Y., Zhang, Y., and Zhao, F.: New Data-driven Estimation of Terrestrial CO₂ fluxes in Asia Using a Standardized Database of Eddy Covariance Measurements, *Remote Sensing Data, and Support Vector Regression, Journal of Geophysical Research: Biogeosciences*, 122, 767–795, 2017.

760 Joiner, J. and Yoshida, Y.: Satellite-Based Reflectances Capture Large Fraction of Variability in Global Gross Primary Production (GPP) at Weekly Time Scales, *Agricultural and Forest Meteorology*, 291, 108 092, 2020.



Jung, M., Reichstein, M., and Bondeau, A.: Towards Global Empirical Upscaling of FLUXNET Eddy Covariance Observations: Validation of a Model Tree Ensemble Approach Using a Biosphere Model, *Biogeosciences*, 6, 2001–2013, 2009.

765 Jung, M., Reichstein, M., Margolis, H. A., Cescatti, A., Richardson, A. D., Arain, M. A., Arneth, A., Bernhofer, C., Bonal, D., Chen, J., Ganelle, D., Gobron, N., Kiely, G., Kutsch, W., Lasslop, G., Law, B. E., Lindroth, A., Merbold, L., Montagnani, L., Moors, E. J., Papale, D., Sottocornola, M., Vaccari, F., and Williams, C.: Global Patterns of Land-Atmosphere Fluxes of Carbon Dioxide, Latent Heat, and Sensible Heat Derived from Eddy Covariance, Satellite, and Meteorological Observations, *Journal of Geophysical Research*, 116, 2011.

Jung, M., Reichstein, M., Schwalm, C. R., Huntingford, C., Sitch, S., Ahlström, A., Arneth, A., Camps-Valls, G., Ciais, P., Friedlingstein, P., Gans, F., Ichii, K., Jain, A. K., Kato, E., Papale, D., Poulter, B., Raduly, B., Rödenbeck, C., Tramontana, G., Viovy, N., Wang, Y.-P., Weber, U., Zaehle, S., and Zeng, N.: Compensatory Water Effects Link Yearly Global Land CO₂ Sink Changes to Temperature, *Nature*, 541, 516–520, 2017.

Jung, M., Koirala, S., Weber, U., Ichii, K., Gans, F., Camps-Valls, G., Papale, D., Schwalm, C., Tramontana, G., and Reichstein, M.: The FLUXCOM Ensemble of Global Land-Atmosphere Energy Fluxes, *Scientific Data*, 6, 2019.

775 Jung, M., Schwalm, C., Migliavacca, M., Walther, S., Camps-Valls, G., Koirala, S., Anthoni, P., Besnard, S., Bodesheim, P., Carvalhais, N., Chevallier, F., Gans, F., Goll, D. S., Haverd, V., Köhler, P., Ichii, K., Jain, A. K., Liu, J., Lombardozzi, D., Nabel, J. E. M. S., Nelson, J. A., O’Sullivan, M., Pallandt, M., Papale, D., Peters, W., Pongratz, J., Rödenbeck, C., Sitch, S., Tramontana, G., Walker, A., Weber, U., and Reichstein, M.: Scaling Carbon Fluxes from Eddy Covariance Sites to Globe: Synthesis and Evaluation of the FLUXCOM Approach, *Biogeosciences*, 17, 1343–1365, 2020.

780 Jung, M., Nelson, J., Migliavacca, M., El-Madany, T., Papale, D., Reichstein, M., Walther, S., and Wutzler, T.: Technical Note: Flagging Inconsistencies in Flux Tower Data, 2023.

Klatt, J., Schmid, H. P., Mauder, M., and Steinbrecher, R.: FLUXNET2015 DE-Sfn Schechenfilz Nord, 2016.

Knohl, A., Tiedemann, F., Kolle, O., Schulze, E.-D., Anthoni, P., Kutsch, W., Herbst, M., and Siebicke, L.: FLUXNET2015 DE-Lnf Leinefelde, 2016.

785 Knox, S.: AmeriFlux FLUXNET-1F CA-DB2 Delta Burns Bog 2, 2022.

Kobayashi, H. and Suzuki, R.: FLUXNET2015 US-Prr Poker Flat Research Range Black Spruce Forest, 2016.

Kosugi, Y. and Takanashi, S.: FLUXNET2015 MY-PSO Pasoh Forest Reserve (PSO), 2016.

Kotani, A.: FLUXNET2015 JP-SMF Seto Mixed Forest Site, 2016a.

Kotani, A.: FLUXNET2015 JP-MBF Moshiri Birch Forest Site, 2016b.

790 Kumar, J., Hoffman, F. M., Hargrove, W. W., and Collier, N.: Understanding the Representativeness of FLUXNET for Upscaling carbon Flux from Eddy Covariance Measurements, 2016.

Kurc, S.: AmeriFlux FLUXNET-1F US-SRC Santa Rita Creosote, 2022.

Kusak, K., Sanchez, C., Szutu, D., and Baldocchi, D.: AmeriFlux FLUXNET-1F US-Snf Sherman Barn, 2022.

Kutzbach, L.: AmeriFlux FLUXNET-1F AR-TF1 Rio Moat Bog, 2021.

795 Köhler, P., Frankenberg, C., Magney, T. S., Guanter, L., Joiner, J., and Landgraf, J.: Global Retrievals of Solar-Induced Chlorophyll Fluorescence With TROPOMI: First Results and Intersensor Comparison to OCO-2, *Geophysical Research Letters*, 45, 2018.

Law, B.: FLUXNET2015 US-Me3 Metolius-second Young Aged Pine, 2016a.

Law, B.: FLUXNET2015 US-Me6 Metolius Young Pine Burn, 2016b.

Law, B.: FLUXNET2015 US-Me1 Metolius - Eyerly Burn, 2016c.

800 Law, B.: FLUXNET2015 US-Me5 Metolius-first Young Aged Pine, 2016d.



Law, B.: FLUXNET2015 US-Me4 Metolius-old Aged Ponderosa Pine, 2016e.

Law, B.: AmeriFlux FLUXNET-1F US-Me2 Metolius Mature Ponderosa Pine, 2022.

Liddell, M. J.: FLUXNET2015 AU-Rob Robson Creek, Queensland, Australia, 2016.

Lindauer, M., Steinbrecher, R., Wolpert, B., Mauder, M., and Schmid, H. P.: FLUXNET2015 DE-Lkb Lackenberg, 2016.

805 Litvak, M.: AmeriFlux FLUXNET-1F US-Mpj Mountainair Pinyon-Juniper Woodland, 2021.

Litvak, M.: AmeriFlux FLUXNET-1F US-Wjs Willard Juniper Savannah, 2022.

Liu, H., Huang, M., and Chen, X.: AmeriFlux FLUXNET-1F US-Hn3 Hanford 100H Sagebrush, 2022.

Lohila, A., Aurela, M., Tuovinen, J.-P., Hatakka, J., and Laurila, T.: FLUXNET2015 FI-Jok Jokioinen, 2016.

Lund, M., Jackowicz-Korczyński, M., and Abermann, J.: FLUXNET2015 GL-ZaH Zackenberg Heath, 2016a.

810 Lund, M., Jackowicz-Korczyński, M., and Abermann, J.: FLUXNET2015 GL-ZaF Zackenberg Fen, 2016b.

Macfarlane, C., Lambert, P., Byrne, J., Johnstone, C., and Smart, N.: FLUXNET2015 AU-Gin Gingin, 2016.

Manca, G. and Goded, I.: FLUXNET2015 IT-PT1 Parco Ticino Forest, 2016.

Margolis, H. A.: FLUXNET2015 CA-Qfo Quebec - Eastern Boreal, Mature Black Spruce, 2016.

Martens, B., Miralles, D. G., Lievens, H., van der Schalie, R., de Jeu, R. A. M., Fernández-Prieto, D., Beck, H. E., Dorigo, W. A., and 815 Verhoest, N. E. C.: GLEAM V3: Satellite-Based Land Evaporation and Root-Zone Soil Moisture, *Geoscientific Model Development*, 10, 1903–1925, 2017.

Massman, B.: FLUXNET2015 US-GBT GLEES Brooklyn Tower, 2016.

Massman, B.: AmeriFlux FLUXNET-1F US-GLE GLEES, 2022.

Matamala, R.: FLUXNET2015 US-IB2 Fermi National Accelerator Laboratory- Batavia (Prairie Site), 2016.

820 Matteucci, G.: FLUXNET2015 IT-Col Collelongo, 2016.

McCaughey, H.: FLUXNET2015 CA-Gro Ontario - Groundhog River, Boreal Mixedwood Forest, 2016.

Merbold, L., Rebmann, C., and Corradi, C.: FLUXNET2015 RU-Che Cherski, 2016.

Meyer, W., Cale, P., Koerber, G., Ewenz, C., and Sun, Q.: FLUXNET2015 AU-Cpr Calperum, 2016.

Meyers, T.: FLUXNET2015 US-LWW Little Washita Watershed, 2016a.

825 Meyers, T.: FLUXNET2015 US-Goo Goodwin Creek, 2016b.

Miralles, D. G., Holmes, T. R. H., De Jeu, R. A. M., Gash, J. H., Meesters, A. G. C. A., and Dolman, A. J.: Global Land-Surface Evaporation Estimated from Satellite-Based Observations, *Hydrology and Earth System Sciences*, 15, 453–469, 2011.

Miralles, D. G., Jiménez, C., Jung, M., Michel, D., Ershadi, A., McCabe, M. F., Hirschi, M., Martens, B., Dolman, A. J., Fisher, J. B., Mu, Q., 830 Seneviratne, S. I., Wood, E. F., and Fernández-Prieto, D.: The WACMOS-ET Project – Part 2: Evaluation of Global Terrestrial Evaporation Data Sets, *Hydrology and Earth System Sciences*, 20, 823–842, 2016.

Moncrieff, J., Malhi, Y., and Leuning, R.: The Propagation of Errors in Long-Term Measurements of Land-Atmosphere Fluxes of Carbon and Water, *Global Change Biology*, 2, 231–240, 1996.

Munassar, S., Rödenbeck, C., Koch, F.-T., Totsche, K. U., Gałkowski, M., Walther, S., and Gerbig, C.: Net Ecosystem Exchange (NEE) Estimates 2006–2019 over Europe from a Pre-Operational Ensemble-Inversion System, *Atmospheric Chemistry and Physics*, 22, 7875–835 7892, 2022.

Munger, J. W.: FLUXNET2015 US-Ha1 Harvard Forest EMS Tower (HFR1), 2016.



Musavi, T., Migliavacca, M., Reichstein, M., Kattge, J., Wirth, C., Black, T. A., Janssens, I., Knöhl, A., Loustau, D., Roupsard, O., Varlagin, A., Rambal, S., Cescatti, A., Ganelle, D., Kondo, H., Tamrakar, R., and Mahecha, M. D.: Stand Age and Species Richness Dampen Interannual Variation of Ecosystem-Level Photosynthetic Capacity, *Nature Ecology & Evolution*, 1, 2017.

840 Nash, J. and Sutcliffe, J.: River Flow Forecasting Through Conceptual Models Part I — A Discussion of Principles, *Journal of Hydrology*, 10, 282–290, 1970.

Nelson, J.: Jnelson18/TranspirationEstimationAlgorithm: Small Bug Fixes with Compatability, Zenodo, 2021.

Nelson, J. A., Carvalhais, N., Cuntz, M., Delpierre, N., Knauer, J., Ogée, J., Migliavacca, M., Reichstein, M., and Jung, M.: Coupling Water and Carbon Fluxes to Constrain Estimates of Transpiration: The TEA Algorithm, *Journal of Geophysical Research: Biogeosciences*, 123, 845 3617–3632, 2018.

Nelson, J. A., Pérez-Priego, O., Zhou, S., Poyatos, R., Zhang, Y., Blanken, P. D., Gimeno, T. E., Wohlfahrt, G., Desai, A. R., Gioli, B., Limousin, J., Bonal, D., Paul-Limoges, E., Scott, R. L., Varlagin, A., Fuchs, K., Montagnani, L., Wolf, S., Delpierre, N., Berveiller, D., Gharun, M., Belelli Marchesini, L., Ganelle, D., Šigut, L., Mammarella, I., Siebicke, L., Andrew Black, T., Knöhl, A., Hörtig, L., Magliulo, V., Besnard, S., Weber, U., Carvalhais, N., Migliavacca, M., Reichstein, M., and Jung, M.: Ecosystem Transpiration and Evaporation: Insights from Three Water Flux Partitioning Methods Across FLUXNET Sites, *Global Change Biology*, 26, 6916–6930, 850 2020.

Network), N.: AmeriFlux FLUXNET-1F US-xBR NEON Bartlett Experimental Forest (BART), 2022.

Nouvellon, Y.: FLUXNET2015 CG-Tch Tchizalamou, 2016.

Novick, K. and Phillips, R.: AmeriFlux FLUXNET-1F US-MMS Morgan Monroe State Forest, 2022.

855 Novick, K. A., Metzger, S., Anderegg, W. R. L., Barnes, M., Cala, D. S., Guan, K., Hemes, K. S., Hollinger, D. Y., Kumar, J., Litvak, M., Lombardozzi, D., Normile, C. P., Oikawa, P., Runkle, B. R. K., Torn, M., and Wiesner, S.: Informing Nature-based Climate Solutions for the United States with the Best-available Science, *Global Change Biology*, 28, 3778–3794, 2022.

Oikawa, P.: AmeriFlux FLUXNET-1F US-EDN Eden Landing Ecological Reserve, 2021.

Olesen, J.: FLUXNET2015 DK-Fou Foulom, 2016.

860 Ourcival, J.-M.: FLUXNET2015 FR-Pue Puechabon, 2016.

Papale, D. and Valentini, R.: A New Assessment of European Forests Carbon Exchanges by Eddy Fluxes and Artificial Neural Network Spatialization, *Global Change Biology*, 9, 525–535, 2003.

Papale, D., Black, T. A., Carvalhais, N., Cescatti, A., Chen, J., Jung, M., Kiely, G., Lasslop, G., Mahecha, M. D., Margolis, H., Merbold, L., Montagnani, L., Moors, E., Olesen, J. E., Reichstein, M., Tramontana, G., Gorsel, E., Wohlfahrt, G., and Ráduly, B.: Effect of Spatial 865 Sampling from European Flux Towers for Estimating Carbon and Water Fluxes with Artificial Neural Networks, *Journal of Geophysical Research: Biogeosciences*, 120, 1941–1957, 2015.

Papale, D., Tirone, G., Valentini, R., Arriga, N., Belelli, L., Consalvo, C., Dore, S., Manca, G., Mazzenga, F., Sabbatini, S., and Stefani, P.: FLUXNET2015 IT-Ro2 Roccarespampani 2, 2016.

Pastorello, G., Trotta, C., Canfora, E., Chu, H., Christianson, D., Cheah, Y.-W., Poindexter, C., Chen, J., Elbashandy, A., Humphrey, M., 870 Isaac, P., Polidori, D., Reichstein, M., Ribeca, A., van Ingen, C., Vuichard, N., Zhang, L., Amiro, B., Ammann, C., Arain, M. A., Ardö, J., Arkebauer, T., Arndt, S. K., Arriga, N., Aubinet, M., Aurela, M., Baldocchi, D., Barr, A., Beamesderfer, E., Marchesini, L. B., Bergeron, O., Beringer, J., Bernhofer, C., Berveiller, D., Billesbach, D., Black, T. A., Blanken, P. D., Bohrer, G., Boike, J., Bolstad, P. V., Bonal, D., Bonnefond, J.-M., Bowling, D. R., Bracho, R., Brodeur, J., Brümmer, C., Buchmann, N., Burban, B., Burns, S. P., Buysse, P., Cale, P., Cavagna, M., Cellier, P., Chen, S., Chini, I., Christensen, T. R., Cleverly, J., Collalti, A., Consalvo, C., Cook, B. D., Cook, D., Coursolle, C.,



875 Cremonese, E., Curtis, P. S., D'Andrea, E., da Rocha, H., Dai, X., Davis, K. J., Cinti, B. D., Grandcourt, A. d., Ligne, A. D., De Oliveira, R. C., Delpierre, N., Desai, A. R., Di Bella, C. M., Tommasi, P. d., Dolman, H., Domingo, F., Dong, G., Dore, S., Duce, P., Dufrêne, E., Dunn, A., Dušek, J., Eamus, D., Eichelmann, U., ElKhidir, H. A. M., Eugster, W., Ewenz, C. M., Ewers, B., Famulari, D., Fares, S., Feigenwinter, I., Feitz, A., Fensholt, R., Filippa, G., Fischer, M., Frank, J., Galvagno, M., Gharun, M., Gianelle, D., Gielen, B., Gioli, B., Gitelson, A., Goded, I., Goeckede, M., Goldstein, A. H., Gough, C. M., Goulden, M. L., Graf, A., Griebel, A., Gruening, C., Grünwald, T., Hammerle, A., Han, S., Han, X., Hansen, B. U., Hanson, C., Hatakka, J., He, Y., Hehn, M., Heinesch, B., Hinko-Najera, N., Hörtnagl, L., Hutley, L., Ibrom, A., Ikawa, H., Jackowicz-Korczynski, M., Janouš, D., Jans, W., Jassal, R., Jiang, S., Kato, T., Khomik, M., Klatt, J., Knohl, A., Knox, S., Kobayashi, H., Koerber, G., Kolle, O., Kosugi, Y., Kotani, A., Kowalski, A., Kruijt, B., Kurbatova, J., Kutsch, W. L., Kwon, H., Launiainen, S., Laurila, T., Law, B., Leuning, R., Li, Y., Liddell, M., Limousin, J.-M., Lion, M., Liska, A. J., Lohila, A., López-Ballesteros, A., López-Blanco, E., Loubet, B., Loustau, D., Lucas-Moffat, A., Lüters, J., Ma, S., Macfarlane, C., Magliulo, V., Maier, R., Mammarella, I., Manca, G., Marcolla, B., Margolis, H. A., Marras, S., Massman, W., Mastepanov, M., Matamala, R., Matthes, J. H., Mazzenga, F., McCaughey, H., McHugh, I., McMillan, A. M. S., Merbold, L., Meyer, W., Meyers, T., Miller, S. D., Minerbi, S., Moderow, U., Monson, R. K., Montagnani, L., Moore, C. E., Moors, E., Moreaux, V., Moureaux, C., Munger, J. W., Nakai, T., Neirynck, J., Nesic, Z., Nicolini, G., Noormets, A., Northwood, M., Nosetto, M., Nouvellon, Y., Novick, K., Oechel, W., Olesen, J. E., Ourcival, J.-M., Papuga, S. A., Parmentier, F.-J., Paul-Limoges, E., Pavelka, M., Peichl, M., Pendall, E., Phillips, R. P., Pilegaard, K., Pirk, N., Posse, G., Powell, T., Prasse, H., Prober, S. M., Rambal, S., Rannik, , Raz-Yaseef, N., Rebmann, C., Reed, D., Dios, V. R. d., Restrepo-Coupe, N., Reverter, B. R., Roland, M., Sabbatini, S., Sachs, T., Saleska, S. R., Sánchez-Cañete, E. P., Sanchez-Mejia, Z. M., Schmid, H. P., Schmidt, M., Schneider, K., Schrader, F., Schroder, I., Scott, R. L., Sedlák, P., Serrano-Ortíz, P., Shao, C., Shi, P., Shironya, I., Siebicke, L., Šigut, L., Silberstein, R., Sirca, C., Spano, D., Steinbrecher, R., Stevens, R. M., Sturtevant, C., Suyker, A., Tagesson, T., Takanashi, S., Tang, Y., Tapper, N., Thom, J., Tomassucci, M., Tuovinen, J.-P., Urbanski, S., Valentini, R., van der Molen, M., van Gorsel, E., van Huissteden, K., Varlagin, A., Verfaillie, J., Vesala, T., Vincke, C., Vitale, D., Vygodskaya, N., Walker, J. P., Walter-Shea, E., Wang, H., Weber, R., Westermann, S., Wille, C., Wofsy, S., Wohlfahrt, G., Wolf, S., Woodgate, W., Li, Y., Zampedri, R., Zhang, J., Zhou, G., Zona, D., Agarwal, D., Biraud, S., Torn, M., and Papale, D.: The FLUXNET2015 Dataset and the ONEFlux Processing Pipeline for Eddy Covariance Data, *Scientific Data*, 7, 225, 2020.

880 Pendall, E. and Griebel, A.: FLUXNET2015 AU-Cum Cumberland Plains, 2016.

885 900 Pilegaard, K. and Ibrom, A.: FLUXNET2015 DK-Eng Enghave, 2016.

Posse, G., Lewczuk, N., Richter, K., and Cristiano, P.: FLUXNET2015 AR-Vir Virasoro, 2016.

Poveda, F. D., Ballesteros, A. L., Cañete, E. P. S., Ortiz, P. S., Jiménez, M. R. M., Priego, O. P., and Kowalski, A. S.: FLUXNET2015 ES-Amo Amoladeras, 2016.

Priestley, C. H. B. and Taylor, R. J.: On the Assessment of Surface Heat Flux and Evaporation Using Large-Scale Parameters, *Monthly Weather Review*, 100, 81–92, 1972.

905 Randerson, J., Van der werf, G., Giglio, L., Collatz, G., and Kasibhatla, P.: Global Fire Emissions Database, Version 4.1 (GFEDv4), 2017.

Reichstein, M., Falge, E., Baldocchi, D., Papale, D., Aubinet, M., Berbigier, P., Bernhofer, C., Buchmann, N., Gilmanov, T., Granier, A., Grunwald, T., Havrankova, K., Ilvesniemi, H., Janous, D., Knohl, A., Laurila, T., Lohila, A., Loustau, D., Matteucci, G., Meyers, T., Miglietta, F., Ourcival, J.-M., Pumpanen, J., Rambal, S., Rotenberg, E., Sanz, M., Tenhunen, J., Seufert, G., Vaccari, F., Vesala, T., Yakir, D., and Valentini, R.: On the Separation of Net Ecosystem Exchange into Assimilation and Ecosystem Respiration: Review and Improved Algorithm, *Global Change Biology*, 11, 1424–1439, 2005.



Reichstein, M., Camps-Valls, G., Stevens, B., Jung, M., Denzler, J., Carvalhais, N., and Prabhat: Deep Learning and Process Understanding for Data-Driven Earth System Science, *Nature*, 566, 195–204, 2019.

Reverter, B. R., Perez-Cañete, E. S., and Kowalski, A. S.: FLUXNET2015 ES-Ln2 Lanjaron-Salvage Logging, 2016a.

915 Reverter, B. R., Perez-Cañete, E. S., and Kowalski, A. S.: FLUXNET2015 ES-LgS Laguna Seca, 2016b.

Rey-Sánchez, C., Wang, C., Szutu, D., Hemes, K., Verfaillie, J., and Baldocchi, D.: AmeriFlux FLUXNET-1F US-Bi2 Bouldin Island Corn, 2022a.

Rey-Sánchez, C., Wang, C., Szutu, D., Shortt, R., Chamberlain, S., Verfaillie, J., and Baldocchi, D.: AmeriFlux FLUXNET-1F US-Bi1 Bouldin Island Alfalfa, 2022b.

920 RI, I.: Ecosystem Final Quality (L2) Product in ETC-Archive Format - Release 2021-1, 2021.

RI, I.: Ecosystem Final Quality (L2) Product in ETC-Archive Format - Release 2022-1, 2022.

Roedenbeck, C. and Heimann, M.: Jena CarboScope: Atmospheric CO₂ Inversion, 2022.

Rödenbeck, C., Zaehle, S., Keeling, R., and Heimann, M.: How Does the Terrestrial Carbon Exchange Respond to Inter-Annual Climatic Variations? A Quantification Based on Atmospheric CO₂ Data, *Biogeosciences*, 15, 2481–2498, 2018.

925 Sabbatini, S., Arriga, N., Gioli, B., and Papale, D.: FLUXNET2015 IT-CA2 Castel d'Asso2, 2016a.

Sabbatini, S., Arriga, N., Matteucci, G., and Papale, D.: FLUXNET2015 IT-CA3 Castel d'Asso 3, 2016b.

Sabbatini, S., Arriga, N., and Papale, D.: FLUXNET2015 IT-CA1 Castel d'Asso1, 2016c.

Sachs, T., Wille, C., Larmanou, E., and Franz, D.: FLUXNET2015 DE-Zrk Zarnekow, 2016.

930 Saleska, S.: FLUXNET2015 BR-Sa1 Santarem-Km67-Primary Forest, 2016.

Sanchez, C. R., Sturtevant, C., Szutu, D., Baldocchi, D., Eichelmann, E., and Knox, S.: FLUXNET2015 US-Tw4 Twitchell East End Wetland, 2016.

Schaaf, C. and Wang, Z.: MCD43A2 MODIS/Terra+Aqua BRDF/Albedo Quality Daily L3 Global - 500m V006, 2015a.

Schaaf, C. and Wang, Z.: MCD43A4 MODIS/Terra+Aqua BRDF/Albedo Nadir BRDF Adjusted Ref Daily L3 Global - 500m V006, 2015b.

935 Schlesinger, W. H. and Jasechko, S.: Transpiration in the Global Water Cycle, *Agricultural and Forest Meteorology*, 189–190, 115–117, 2014.

Schneider, K. and Schmidt, M.: FLUXNET2015 DE-Seh Selhausen, 2016.

Schneider, U., Hänsel, S., Finger, P., Rustemeier, E., and Ziese, M.: GPCC Full Data Monthly Version 2022 at 0.25°: Monthly Land-Surface Precipitation from Rain-Gauges Built on GTS-based and Historic Data, 2022.

Schroder, I., Zegelin, S., Palu, T., and Feitz, A.: FLUXNET2015 AU-Emr Emerald, 2016.

940 Scott, R.: FLUXNET2015 US-SRG Santa Rita Grassland, 2016a.

Scott, R.: FLUXNET2015 US-SRM Santa Rita Mesquite, 2016b.

Scott, R.: FLUXNET2015 US-Wkg Walnut Gulch Kendall Grasslands, 2016c.

Scott, R.: FLUXNET2015 US-Whs Walnut Gulch Lucky Hills Shrub, 2016d.

Shao, C.: FLUXNET2015 CN-Sw2 Siziwang Grazed (SZWG), 2016a.

945 Shao, C.: FLUXNET2015 CN-Du3 Duolun Degraded Meadow, 2016b.

Shi, P., Zhang, X., and He, Y.: FLUXNET2015 CN-Dan Dangxiong, 2016.

Shortt, R., Hemes, K., Szutu, D., Verfaillie, J., and Baldocchi, D.: AmeriFlux FLUXNET-1F US-Sne Sherman Island Restored Wetland, 2022.

Sigut, L., Havrankova, K., Jocher, G., Pavelka, M., and Janouš, D.: FLUXNET2015 CZ-BK2 Bily Kriz Grassland, 2016.



950 Silveira, M.: AmeriFlux FLUXNET-1F US-ONA Florida Pine Flatwoods, 2021.
Spano, D., Duce, P., Marras, S., Sirca, C., Arca, A., Zara, P., and Ventura, A.: FLUXNET2015 IT-Noe Arca Di Noe - Le Prigionette, 2016.
Staebler, R.: AmeriFlux FLUXNET-1F CA-Cbo Ontario - Mixed Deciduous, Borden Forest Site, 2022.
Sturtevant, C., Szutu, D., Baldocchi, D., Matthes, J. H., Oikawa, P., and Chamberlain, S. D.: FLUXNET2015 US-Myb Mayberry Wetland, 2016.

955 Sturtevant, C., Verfaillie, J., and Baldocchi, D.: AmeriFlux FLUXNET-1F US-Tw2 Twitchell Corn, 2022.
Suyker, A.: FLUXNET2015 US-Ne3 Mead - Rainfed Maize-Soybean Rotation Site, 2016a.
Suyker, A.: FLUXNET2015 US-Ne2 Mead - Irrigated Maize-Soybean Rotation Site, 2016b.
Suyker, A.: AmeriFlux FLUXNET-1F US-Ne1 Mead - Irrigated Continuous Maize Site, 2022.
Tagesson, T., Ardö, J., and Fensholt, R.: FLUXNET2015 SN-Dhr Dahra, 2016.

960 Tang, Y., Kato, T., and Du, M.: FLUXNET2015 CN-HaM Haibei Alpine Tibet Site, 2016.
Team, D. . and Centre, I. E. T.: Drought-2018 Ecosystem Eddy Covariance Flux Product for 52 Stations in FLUXNET-Archive Format, 2020.
Team, W. W. . and Centre, I. E. T.: Warm Winter 2020 Ecosystem Eddy Covariance Flux Product for 73 Stations in FLUXNET-Archive Format—Release 2022-1, 2022.

965 Torn, M.: FLUXNET2015 US-ARc ARM Southern Great Plains Control Site- Lamont, 2016a.
Torn, M.: FLUXNET2015 US-ARb ARM Southern Great Plains Burn Site- Lamont, 2016b.
Torn, M. and Dengel, S.: AmeriFlux FLUXNET-1F US-NGB NGEE Arctic Barrow, 2021.
Tramontana, G., Jung, M., Schwalm, C. R., Ichii, K., Camps-Valls, G., Ráduly, B., Reichstein, M., Arain, M. A., Cescatti, A., Kiely, G., Merbald, L., Serrano-Ortiz, P., Sickert, S., Wolf, S., and Papale, D.: Predicting Carbon Dioxide and Energy Fluxes Across Global FLUXNET Sites with regression Algorithms, *Biogeosciences*, 13, 4291–4313, 2016.

970 Turner, D. P., Ritts, W. D., Cohen, W. B., Gower, S. T., Running, S. W., Zhao, M., Costa, M. H., Kirschbaum, A. A., Ham, J. M., Saleska, S. R., and Ahl, D. E.: Evaluation of MODIS NPP and GPP Products Across Multiple Biomes, *Remote Sensing of Environment*, 102, 282–292, 2006.

Ukkola, A. M., Abramowitz, G., and De Kauwe, M. G.: A Flux Tower Dataset Tailored for Land Model Evaluation, *Earth System Science Data*, 14, 449–461, 2022.

975 Upton, S., Reichstein, M., Gans, F., Peters, W., Kraft, B., and Bastos, A.: Constraining Biospheric Carbon Dioxide Fluxes by Combined Top-down and Bottom-up Approaches, 2023.

Valach, A., Shortt, R., Szutu, D., Eichelmann, E., Knox, S., Hemes, K., Verfaillie, J., and Baldocchi, D.: AmeriFlux FLUXNET-1F US-Tw1 Twitchell Wetland West Pond, 2021.

Valach, A., Kasak, K., Szutu, D., Verfaillie, J., and Baldocchi, D.: AmeriFlux FLUXNET-1F US-Tw5 East Pond Wetland, 2022.

980 Valentini, R., Dore, S., Mazzenga, F., Sabbatini, S., Stefani, P., Tirone, G., and Papale, D.: FLUXNET2015 IT-Cpz Castelporziano, 2016a.
Valentini, R., Nicolini, G., Stefani, P., De Grandcourt, A., and Stivanello, S.: FLUXNET2015 GH-Ank Ankasa, 2016b.
Valentini, R., Tirone, G., Vitale, D., Papale, D., Arriga, N., Belelli, L., Dore, S., Manca, G., Mazzenga, F., Pegoraro, E., Sabbatini, S., and Stefani, P.: FLUXNET2015 IT-Ro1 Roccarespampani 1, 2016c.

Virkkala, A., Aalto, J., Rogers, B. M., Tagesson, T., Treat, C. C., Natali, S. M., Watts, J. D., Potter, S., Lehtonen, A., Mauritz, M., Schuur, E. A. G., Kochendorfer, J., Zona, D., Oechel, W., Kobayashi, H., Humphreys, E., Goeckede, M., Iwata, H., Lafleur, P. M., Euskirchen, E. S., Bokhorst, S., Marushchak, M., Martikainen, P. J., Elberling, B., Voigt, C., Biasi, C., Sonnentag, O., Parmentier, F. W., Ueyama, M., Celis, G., St.Louis, V. L., Emmerton, C. A., Peichl, M., Chi, J., Järveoja, J., Nilsson, M. B., Oberbauer, S. F., Torn, M. S., Park, S.,



Dolman, H., Mammarella, I., Chae, N., Poyatos, R., López-Blanco, E., Christensen, T. R., Kwon, M. J., Sachs, T., Holl, D., and Luoto, M.: Statistical Upscaling of Ecosystem CO₂ fluxes Across the Terrestrial Tundra and Boreal Domain: Regional Patterns and Uncertainties, 990 Global Change Biology, 27, 4040–4059, 2021.

Vivoni, E. and Perez-Ruiz, E.: AmeriFlux FLUXNET-1F US-Jo2 Jornada Experimental Range Mixed Shrubland, 2022.

Vourlitis, G., Dalmagro, H., De S. Nogueira, J., Johnson, M., and Arruda, P.: AmeriFlux FLUXNET-1F BR-Npw Northern Pantanal Wetland, 2022.

Wagner-Riddle, C.: AmeriFlux FLUXNET-1F CA-ER1 Elora Research Station, 2021.

995 Walther, S.: README FluxnetEO V2, 2023.

Walther and Besnard, Nelson, J. A., El-Madany, T. S., Migliavacca, M., Weber, U., Carvalhais, N., Ermida, S. L., Brümmer, C., Schrader, F., Prokushkin, A. S., Panov, A. V., and Jung, M.: Technical Note: A View from Space on Global Flux Towers by MODIS and Landsat: The FluxnetEO Data Set, Biogeosciences, 19, 2805–2840, 2022.

Wan, Z., Hook, S., and Hulley, G.: MOD11C1 MODIS/Terra Land Surface Temperature/Emissivity Daily L3 Global 0.05Deg CMG V006, 1000 2015.

Wang, H. and Fu, X.: FLUXNET2015 CN-Qia Qianyanzhou, 2016.

Wei, Z., Yoshimura, K., Wang, L., Miralles, D. G., Jasechko, S., and Lee, X.: Revisiting the Contribution of Transpiration to Global Terrestrial Evapotranspiration, Geophysical Research Letters, 44, 2792–2801, 2017.

Wohlfahrt, G., Hammerle, A., and Hörtnagl, L.: FLUXNET2015 AT-Neu Neustift, 2016.

1005 Wolf, S., Eugster, W., and Buchmann, N.: FLUXNET2015 PA-SPs Sardinilla-Pasture, 2016a.

Wolf, S., Eugster, W., and Buchmann, N.: FLUXNET2015 PA-SPn Sardinilla Plantation, 2016b.

Wood, J. and Gu, L.: AmeriFlux FLUXNET-1F US-MOz Missouri Ozark Site, 2022.

Woodgate, W., Van Gorsel, E., and Leuning, R.: FLUXNET2015 AU-Tum Tumbarumba, 2016.

Xiao, J., Zhuang, Q., Baldocchi, D. D., Law, B. E., Richardson, A. D., Chen, J., Oren, R., Starr, G., Noormets, A., Ma, S., Verma, S. B., 1010 Wharton, S., Wofsy, S. C., Bolstad, P. V., Burns, S. P., Cook, D. R., Curtis, P. S., Drake, B. G., Falk, M., Fischer, M. L., Foster, D. R., Gu, L., Hadley, J. L., Hollinger, D. Y., Katul, G. G., Litvak, M., Martin, T. A., Matamala, R., McNulty, S., Meyers, T. P., Monson, R. K., Munger, J. W., Oechel, W. C., Paw U, K. T., Schmid, H. P., Scott, R. L., Sun, G., Suyker, A. E., and Torn, M. S.: Estimation of Net Ecosystem Carbon Exchange for the Conterminous United States by Combining MODIS and AmeriFlux Data, Agricultural and Forest Meteorology, 148, 1827–1847, 2008.

1015 Yao, Y., Li, Z., Wang, T., Chen, A., Wang, X., Du, M., Jia, G., Li, Y., Li, H., Luo, W., Ma, Y., Tang, Y., Wang, H., Wu, Z., Yan, J., Zhang, X., Zhang, Y., Zhang, Y., Zhou, G., and Piao, S.: A New Estimation of China's Net Ecosystem Productivity Based on Eddy Covariance Measurements and a Model Tree Ensemble Approach, Agricultural and Forest Meteorology, 253-254, 84–93, 2018.

Yepez, E. and Garatuza, J.: AmeriFlux FLUXNET-1F MX-Tes Tesopaco, Secondary Tropical Dry Forest, 2021.

Zhang, J. and Han, S.: FLUXNET2015 CN-Cha Changbaishan, 2016.

1020 Zhang, Y., Xiao, X., Zhang, Y., Wolf, S., Zhou, S., Joiner, J., Guanter, L., Verma, M., Sun, Y., Yang, X., Paul-Limoges, E., Gough, C. M., Wohlfahrt, G., Gioli, B., van der Tol, C., Yann, N., Lund, M., and de Grandcourt, A.: On the Relationship Between Sub-Daily Instantaneous and Daily Total Gross Primary Production: Implications for Interpreting Satellite-Based SIF Retrievals, Remote Sensing of Environment, 205, 276–289, 2018.

Zhao, M. and Running, S. W.: Drought-Induced Reduction in Global Terrestrial Net Primary Production from 2000 Through 2009, Science, 1025 329, 940–943, 2010.



Zhou, G. and Yan, J.: FLUXNET2015 CN-Din Dinghushan, 2016.

Zona, D. and Oechel, W.: FLUXNET2015 US-Atq Atqasuk, 2016a.

Zona, D. and Oechel, W.: FLUXNET2015 US-Ivo Iivotuk, 2016b.

Zscheischler, J., Mahecha, M. D., Avitabile, V., Calle, L., Carvalhais, N., Ciais, P., Gans, F., Gruber, N., Hartmann, J., Herold, M., Ichii, K.,
1030 Jung, M., Landschützer, P., Laruelle, G. G., Lauerwald, R., Papale, D., Peylin, P., Poulter, B., Ray, D., Regnier, P., Rödenbeck, C., Roman-
Cuesta, R. M., Schwalm, C., Tramontana, G., Tyukavina, A., Valentini, R., van der Werf, G., West, T. O., Wolf, J. E., and Reichstein, M.:
Reviews and Syntheses: An Empirical Spatiotemporal Description of the Global Surface–Atmosphere Carbon Fluxes: Opportunities and
Data Limitations, *Biogeosciences*, 14, 3685–3703, 2017.